JOURNAL OF GEOPHYSICAL RESEARCH, VOL. 100, NO. E3, PAGES 5501–5523, MARCH 25, 1995

The sensitivity of the Martian surface pressure and atmospheric mass budget to various parameters: A comparison between numerical simulations and Viking observations

Frédéric Hourdin, François Forget, and Olivier Talagrand

Laboratoire de Météorologie Dynamique du Centre National de la Recherche Scientifique, Ecole Normale Supérieure, Paris, France

Abstract. The sensitivity of the Martian atmospheric circulation to a number of poorly known or strongly varying parameters (surface roughness length, atmospheric optical depth, CO_2 ice albedo, and thermal emissivity) is investigated through experiments performed with the Martian version of the atmospheric general circulation model of Laboratoire de Météorologie Dynamique, with a rather coarse horizontal resolution (a grid with 32 points in longitude and 24 points in latitude). The results are evaluated primarily on the basis of comparisons with the surface pressure records of the Viking mission. To that end, the records are decomposed into long-period seasonal variations due to mass exchange with the polar caps and latitudinal redistribution of mass, and short-period variations due to transient longitudinally propagating waves. The sensitivity experiments include a 5-year control simulation and shorter simulations (a little longer than 1 year) performed with "perturbed" parameter values. The main conclusions are that (1) a change of horizontal resolution (twice as many points in each direction) mostly affects the transient waves, (2) surface roughness lengths have a significant impact on the near-surface wind and, as a matter of consequence, on the latitudinal redistribution of mass, (3) atmospheric dust optical depth has a significant impact on radiative balance and dynamics, and (4) CO_2 ice albedo and thermal emissivity strongly influence mass exchange between the atmosphere and the polar caps. In view of this last conclusion, an automatic procedure is implemented through which the albedo and emissivity of each of the two polar caps are determined, together with the total (i.e., including the caps) atmospheric CO_2 content, in such a way as to get the closest fit of the model to the Viking pressure measurements.

1. Introduction

The meteorology of the planet Mars is probably, after that of Earth, the one which has been most studied and is best understood. This is due, first, to the large number of observations acquired in the seventies on the occasion of several spacecraft missions (the Soviet Mars missions and the American Mariner and Viking missions). In particular, the two Viking landers have recorded near-surface temperature, pressure, and winds over several Martian years. Such records are unique for extraterrestrial planets. The Viking measurements, especially the pressure measurements, contain very instructive information on the global atmospheric circulation. The large-amplitude seasonal oscillations of the pressure are due to the variations of the atmospheric mass (which result from condensation-sublimation of a substantial fraction of the atmospheric carbon dioxide in the polar caps), but also to internal latitudinal mass redistribution. The more rapid oscillations of the surface pressure, with periods of 2 to 5 sols (sols are Martian solar days), are signatures of the transient planetary waves which are present, at least in the northern hemisphere, during autumn and winter. Our relatively good knowledge of the Martian meteorology is also due to the results obtained with atmospheric general circulation models (GCM's). The usefulness of GCM's in this particular instance is certainly due in great part to the similarity of the atmospheric circulations of Earth and Mars. As early as the late sixties, the then recently developed terrestrial GCM of the University of California, Los Angeles, was successfully adapted to Mars [*Leovy and Mintz*, 1969]. The same model, on which various improvements were continuously performed, was later used both for the preparation of the Viking mission and for many studies of the Martian meteorology performed at NASA/Ames Research Cen-

Paper number 94JE03079.
0148-0227/95/94JE-03079$05.00

ter by J. B. Pollack and collaborators [*Pollack et al.*, 1981, 1990, 1993; *Haberle et al.*, 1993; *Barnes et al.*, 1993].

More recently, a new version of the terrestrial GCM of Laboratoire de Météorologie Dynamique (LMD) has been adapted to Mars [*Hourdin*, 1992; *Hourdin et al.*, 1993] . The LMD GCM was the first self-consistent model to simulate the Martian atmospheric circulation over more than a year. Despite the somewhat arbitrary use of an a priori set of model parameters, some of which are poorly known from observation, the model was able to reproduce rather accurately many observed features of the Martian atmosphere, such as the thermal structure derived from Mariner 9 temperature retrievals, and the long- and short-period oscillations of the surface pressure observed by the Viking landers. Moreover, those simulations have shown that the large seasonal pressure variations were not only due, as usually thought until then, to mass exchange between the atmosphere and the polar caps, but were also strongly influenced by internal mass redistribution associated to the atmospheric circulation (*Talagrand et al.* [1991], *Hourdin et al.* [1993], referred to as paper 1 hereinafter, and *Pollack et al.* [1993]).

The present paper, which is a continuation of paper 1, is mainly devoted to sensitivity studies of the LMD model to some very uncertain or strongly varying parameters (surface roughness length, atmospheric optical depth, CO_2 ice albedo, and thermal emissivity) with emphasis on their impact on the atmospheric mass budget and on the meteorological contribution to the annual pressure cycle. Similar studies have already been performed by several authors. *Paige and Ingersoll* [1985], *Wood and Paige* [1992], and *Paige and Wood* [1992] have concentrated on the mass budget with a model of the energetics of the polar caps. *Pollack et al.* [1993] performed a more complete study, since they included in their energy budget model the effect of dynamics (heat transport and meteorological contribution to the pressure variations) using the results of off-line simulations performed with the NASA/Ames GCM on a series of selected short periods. The present work is new in that the sensitivity experiments described here have been performed with a self-consistent GCM allowing for complex feedback between dynamics and diabatic processes.

We try here to answer the following questions: (1) What is the uncertainty in the model resulting from the uncertainties in model parameters or parameterizations? (2) Can the model parameters be constrained from the available observations (and especially from the Viking surface pressure measurements)? (3) What information can be derived from the GCM on the polar processes which dominate the mass cycle?

To that end, we propose simple diagnostics for the Viking pressure measurements, well adapted to the validation of GCMs and to the study of the annual pressure cycle. Those diagnostics are the subject of section 2. We then give in section 3 a brief description of the atmospheric model (already described in paper 1) and present in section 4 a 5-year simulation used afterward as control for the sensitivity experiments. In section 5 we test the uncertainties related to the most uncertain model parameters and, in section 6, we study the impact of the variations of the dust amount in the atmosphere. We take advantage of the high sensitivity of the atmospheric mass budget to the CO_2 ice radiative properties (visible albedo and thermal emissivity) to derive an automatic best fit procedure to the Viking pressure. This procedure and the best fit results are presented in section 7.

2. Analysis of the Viking Surface Pressure Measurements

The records of the surface pressure, acquired over almost 2 Martian years by the Viking 2 lander, and over more than 3 years by the Viking 1 lander [*Tillman and Guest*, 1987] , have been widely used for studies of the Martian transient planetary waves [*Tillman*, 1988; *Barnes*, 1980, 1981], for comparisons with the results of seasonal energy balance models [*Pollack et al.*, 1993; *Paige and Ingersoll*, 1985; *Wood and Paige*, 1992; *Paige and Wood*, 1992] , and, in paper 1, for direct comparisons with GCM simulations. We present here simple diagnostics, well suited to GCM validations, based on a decomposition of the observed variations between a seasonal component (which is itself decomposed into a total atmospheric mass contribution and a meteorological contribution) and a shorter term transient component. In the present paper, which does not discuss diurnal cycle and the associated thermal tides (known to be very strong on Mars), we use directly the diurnally averaged pressure data.

Seasonal Variations

The large-amplitude seasonal variations of the surface pressure can easily be isolated, as proposed by *Tillman et al.* [1993], by retaining the first harmonics of the annual cycle. Following the same authors, we retain only the observations performed after the 1977-B dust storm (clear-sky conditions), but we use solar longitude L_S instead of real time t as the temporal variable of our Fourier analysis. L_S is a more appropriate coordinate for the seasonal cycle, since both the inclination of the planet, $\sin\delta = \sin L_S \sin\delta_0$ (where $\delta_0 \sim 24^o$ is the Martian obliquity), and the distance to the sun, $r = p/(1 + e\cos L_S) \sim p(1 - e\cos L_S)$ (where $p = 1.51$ UA and $e = 0.093$), are almost first harmonics of a year in terms of solar longitude (and not in terms of real time).

The values of the amplitude and phase lag of the first eight harmonics are given in Table 1 for the two Viking landers. The quality of the fit (measured from the root mean square of the difference between the data and the synthetic spectra) reaches a minimum value for $N \geq 5$, the residual value corresponding to the mean amplitude of the transient oscillations (about 0.04 mbar for Viking 1 and 0.1 mbar for Viking 1). Somewhat arbitrarily, the eight-harmonic fit (compared to Viking data

Table 1. Amplitude ($p^{(k)}$) and Phase Lag ($L_S^{(k)}$, Solar Longitude of the Maximum Pressure) of the First Eight Harmonics of the Seasonal Pressure Variations Observed by the Viking Landers (Clear-Sky Conditions)

Site	Mode k	$p^{(k)}$, mbar	$L_S^{(k)}$, deg	Mean Quadratic Error ϵ, mbar
VL1	0	7.9623		
	1	0.6887	310.97	
	2	0.5453	66.76	0.0501
	3	0.0154	20.87	0.0512
	4	0.0535	68.53	0.0389
	5	0.0105	33.36	0.0383
	6	0.0053	12.02	0.0378
	7	0.0058	19.85	0.0376
	8	0.0025	13.11	0.0376
VL2	0	8.6889		
	1	0.8320	308.07	
	2	0.6061	66.62	0.1139
	3	0.0422	25.48	0.1120
	4	0.0231	71.05	0.1104
	5	0.0355	65.98	0.1086
	7	0.0119	46.37	0.1081
	8	0.0122	28.59	0.1081

ϵ is the mean quadratic difference between the Viking individual data and the synthetic values reconstructed from the first N harmonics:

$$p^{[N]}(n) = \sum_{k=0}^{k=N} p^{(k)} \cos\left[k \times \left(L_S - L_S^{(k)}\right)\right]$$

in Figure 1) is retained as a reference seasonal pressure cycle in the present study and used for direct comparison with simulated pressures. However, for both landing sites, the first two harmonics explain the main part of the seasonal variations. Note that the two-harmonic fit is much better when solar longitude is used instead of real time as a spectral coordinate. For the time coordinate, for instance, the amplitude of the third harmonic at Viking 1 is of the order of 0.1 mbar, and the root mean square of the difference between the two-harmonic fit and the data is of the order of 0.075 mbar.

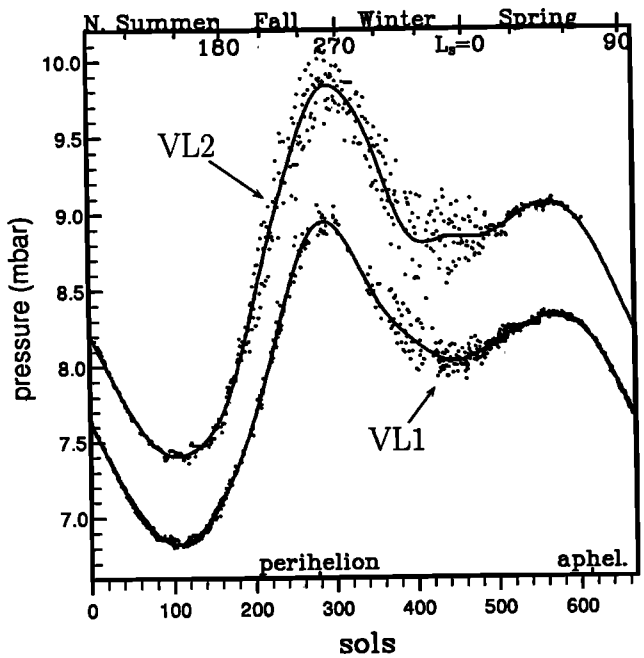

Figure 1. Diurnally averaged Viking pressure observations for clear-sky conditions (points) are compared to the eight-harmonic L_S fit (solid curve).

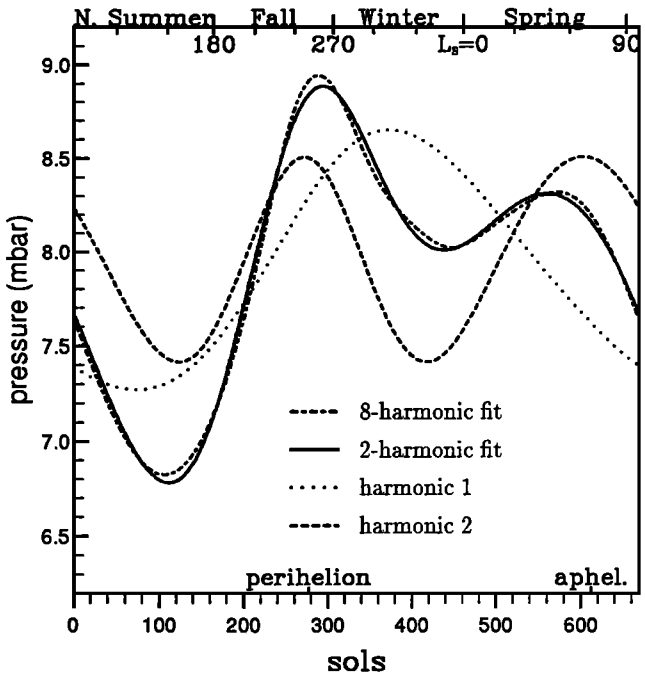

Figure 2. Two- and eight-harmonic fits of the time evolution of the surface pressure observations at Viking 1. The reference eight-harmonic fit is already shown in Figure 1.

As illustrated in Figure 2 and Table 1, harmonic 2 really corresponds to the seasonal cycle with two minima during the two winters, lagging the solstices by about 66°. The minimum of insolation on one hemisphere at winter solstice corresponds to the maximum condensation rate, the maximum mass of the corresponding cap occurring much later. Harmonic 1 reflects the asymmetry between both winters: mainly forced by orbital eccentricity, it can also be affected by hemispheric asymmetries in orography, in the dust content, and in cloud coverage over caps or amplified by albedo feedbacks on the polar caps. The maximum pressure of the first harmonic also lags the maximum planetary insolation, at perihelion, by about 60°.

Various Contributions to the Local Seasonal Pressure Variations

As discussed above, the seasonal pressure variations are due in part to the variations of the total atmospheric mass M_{atm} resulting from the mass exchange between the polar caps and the atmosphere. It is convenient to introduce the planetary mean of the surface pressure $p_{\text{atm}} = gM_{\text{atm}}/\left(4\pi a^2\right)$, where a is the planetary radius and g the gravity, and to define in the same way an equivalent surface pressure for the northern and southern polar caps, p_N and p_S respectively, and a total

pressure $p_{tot} = p_{atm} + p_N + p_S$, which is independent of time.

However, as first pointed out by *Talagrand et al.* [1991], and studied in greater details in paper 1 and by *Pollack et al.* [1993], the seasonal evolution of the surface pressure at a particular point of the planet can differ significantly, under the effect of latitudinal mass redistribution, from the evolution of the mean surface pressure p_{atm}. It is convenient to introduce here the ratio α of the local pressure to the mean atmospheric surface pressure. This ratio will be called the "meteorological factor" hereafter. As shown in paper 1, the horizontal variations of α can be accurately decomposed into the sum of an orographic and a dynamical component. The orographic component (accounting for the horizontal pressure variations along slopes) varies in time because of the strong seasonal variations of temperature. The dynamical component is due to the geostrophic balance between the surface pressure and the near-surface horizontal winds. It is particularly responsible for strong latitudinal pressure variations in balance with the strong Martian zonal winds. Those zonal winds are produced themselves by latitudinal angular momentum redistribution by the condensation flow and thermally driven atmospheric circulation.

The absolute meteorological contribution cannot be deduced from Viking observations. However, the relative meteorological factor between the two Viking sites, defined as

$$\alpha_{VL2/1} = \frac{p_{VL2} - p_{VL1}}{p_{VL2} + p_{VL1}} = \frac{\alpha_{VL2} - \alpha_{VL1}}{\alpha_{VL2} + \alpha_{VL1}} \quad (1)$$

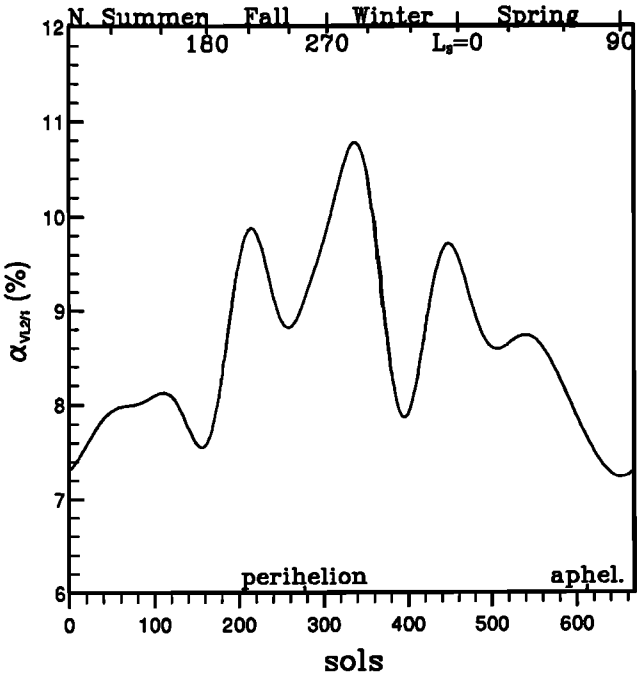

Figure 3. Meteorological contribution to the relative difference between the Viking 2 and Viking 1 pressures $\alpha_{VL2/1} = (p_{VL2} - p_{VL1}) / (p_{VL2} + p_{VL1})$ computed from the eight-harmonic fits.

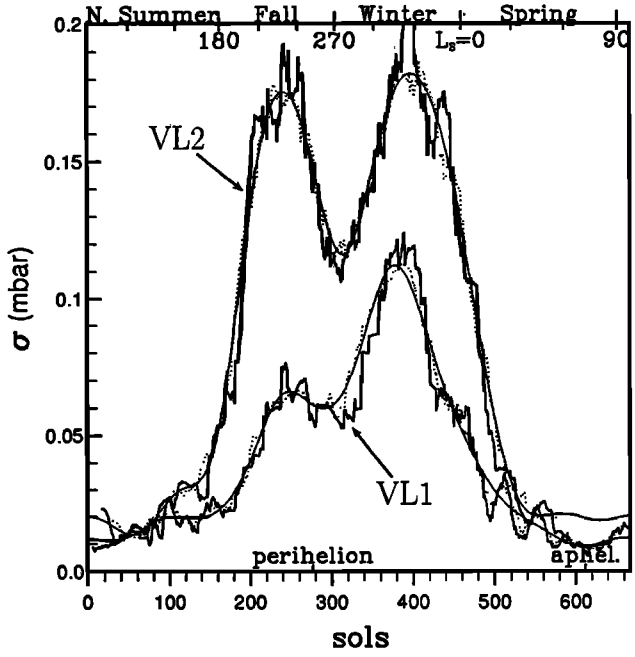

Figure 4. Seasonal evolution of the amplitude of the transient pressure oscillations at both Viking sites computed as the running quadratic mean over 25 (thick solid curve) and 50 (dotted curve) consecutive sols of the difference between the instantaneous (diurnally averaged) Viking pressure and the eight-harmonic fit. The thin solid curve is the eight-harmonic L_S fit to the dotted curve.

can be used for model validation. Figure 3 shows the relative meteorological factor as computed from the eight-harmonic fits to the Viking 1 and Viking 2 data. The maximum of the curve near northern winter solstice can be explained by the very cold temperatures which strongly enhance the pressure in the lowest Viking 2 site. This effect is partly compensated by the presence of the strong winter jet which should correspond by geostrophic balance to a northward decreasing pressure. As explained in paper 1, the disappearance of the near-surface westerlies during the great 1977-B dust storm ($L_S \sim 280$) was responsible for a sudden increase of the surface pressure recorded by the Viking 2 lander.

It is noteworthy that models must be used in addition to observations of the surface pressure in order to deduce the evolution of the atmospheric mass which requires the knowledge of the absolute meteorological factor. The relative factor $\alpha_{VL2/1}$ can only help for the model validation.

Transient Eddies

Another important feature of the observed pressure variations is the presence of short-period fluctuations linked to transient planetary waves. Without going into a complete study of these transient waves, which would require the use of more sophisticated analysis techniques, we can easily determine the seasonal evolution of the amplitude of the transient oscillations by retaining the running quadratic mean, σ_N, over N con-

secutive data, of the difference between the pressure observation for a given sol and the corresponding value computed from the eight-harmonic reference pressure cycle. In order that the seasonal amplitude of the transient waves, but nothing else, be retained in the running mean, the value of N must be significantly larger than the period of the transient waves, and significantly smaller than the length of seasons. As already stated, the analysis is based on diurnally averaged data and thus the transient eddies do not account for the thermal tides.

In Figure 4 we show the time evolution of σ_{25} (thick solid curve) and σ_{50} (dotted curve), which appear to be very similar. For diagnostics, we will retain the eight-harmonic fit to σ_{50} (thin solid line).

Transient eddies occur from northern autumn equinox to early northern spring. The amplitude of the perturbations at the Viking 2 site is about twice that at Viking 1 and shows a two-peak structure with a relative minimum at northern winter solstice.

3. Model

General Description

The LMD Martian GCM has been described in paper 1. The dynamical part is based on a finite difference formulation of the "primitive equations" of meteorology developed for the Terrestrial GCM of LMD [*Sadourny and Laval*, 1984] . We use a more recent formulation (developed by R. Sadourny and P. Le Van and described by F. Hourdin and O. Talagrand, Superrotation of planetary atmospheres: A numerical study, submitted to *Journal of Atmospheric Science*, 1994) which allows us to change automatically the distribution of grid points in longitude and/or latitude. The formulation exactly conserves (1) the total atmospheric mass (in absence of CO_2 condensation), (2) the potential enthalpy and its square for adiabatic motions, (3) the potential enstrophy for barotropic flows, and (4) the total angular momentum for axisymmetric flows.

The physical part has already been presented in detail in paper 1: (1) the radiative transfer is computed using a code adapted by *Hourdin* [1992] from the code currently used at the European Center for Medium-Range Weather Forecasts (ECMWF) [*Fouquart and Bonnel*, 1980; *Morcrette et al.*, 1986] ; it includes absorption and emission by carbon dioxide and dust in the thermal infrared and absorption and scattering by dust in the visible; (2) a simple formulation is used for the vertical turbulent mixing in the whole atmosphere; (3) vertically unstable profiles are prevented by applying a vertical convective adjustment which conserves energy; momentum is also mixed in the unstable layer, the intensity of the mixing depending on the intensity of the vertical instability; (4) the temperature of the surface is computed using an 11–level model of thermal conduction in the soil which correctly simulates the response for oscillatory forcing with periods going from a tenth of day up to a few years; (5) condensation and sublimation of carbon dioxide are computed in a simple energy and mass conserving manner. If somewhere in the atmosphere, the temperature falls below the condensation temperature T_{CO_2}, condensation occurs in an amount appropriate to restore T_{CO_2} by latent heat release. All the condensed CO_2 is assumed to precipitate instantly to the ground, the surface pressure being consequently modified. At the surface, the temperature of the frost is kept at the condensation value either by condensing atmospheric CO_2 or by sublimating CO_2 ice.

The approximation for the pressure-vapor curve used in paper 1 is replaced by a more accurate relationship based on the Clausius-Clapeyron relation for perfect gas. Assuming that the latent heat of sublimation L is independent of temperature, the vapor pressure curve reduces to

$$\ln(p/p_0) = \frac{L}{R}\left(\frac{1}{T_0} - \frac{1}{T_{CO_2}}\right) \tag{2}$$

(where R is the gas constant and T_0 is the condensation temperature corresponding to the pressure chosen as a reference, here $p_0 = 1$ mbar). $L = 5.9 \times 10^5$ J kg^{-1} and $T_0 = 136.3$ K are fixed in the range of experimental values [e.g., *James et al.*, 1992] . The change of the pressure-vapor curve was found to have a minor effect on the atmospheric mass budget.

The only significant change with respect to paper 1 is linked to the diurnal cycle. It was intentionally turned off in the previous study. Here, the radiative forcing is computed about 40 times per day. It then becomes necessary to introduce the dependency of the surface drag coefficient (a constant in paper 1) with both the magnitude of wind and vertical stability above the surface which are known to vary significantly between night and day. In the new version, we use the formulation developed by *Louis* [1979] for the terrestrial planetary boundary layer, in the form which has been implemented at ECMWF.

The drag coefficient is given by

$$C = \left(\frac{k}{\ln \frac{z}{z_0}}\right)^2 f\left(R_i, \frac{z}{z_0}\right) \tag{3}$$

where z_0 is the roughness length, z is the height of the middle of the first atmospheric layer, $k = 0.4$ is the von Karman constant, and

$$R_i = \frac{gz(\theta - T_s)}{\theta ||V||^2} \tag{4}$$

is the Richardson number, where $\theta = T(p_s/p)^{\kappa}$ and $||V||$ are the potential temperature and wind velocity in the first atmospheric layer and T_s the surface temperature. Two different functions f are used for momentum (f_m) and potential temperature (f_θ). In either case, a different formulation is used, depending on whether the atmosphere is stable ($R_i > 0$),

$$f_m = \frac{1}{1 + 2bR_i/\sqrt{1 + dR_i}} \tag{5}$$

$$f_\theta = \frac{1}{1 + 3bR_i\sqrt{1 + dR_i}} \quad (6)$$

or unstable ($R_i < 0$),

$$f_m = 1 - \frac{3bR_i}{1 + 3bC\left[k/\ln(z/z_0)\right]^2\sqrt{-R_i(1 + z/z_0)}} \quad (7)$$

$$f_\theta = 1 - \frac{3bR_i}{1 + 3bC\left[k/\ln(z/z_0)\right]^2\sqrt{-R_i z/z_0}} \quad (8)$$

As in the original terrestrial version, we use $C = b = d = 5$.

Grid

As in paper 1, we use two different horizontal resolutions in the present study: a low horizontal resolution based on a grid with 24 points in latitude and 32 points in longitude and a high resolution with 48 points in latitude and 64 points in longitude. In the vertical, the atmosphere is discretized using 15 σ-levels (σ is the pressure normalized by its surface value $\sigma = p/p_s$), the distribution of which is given in paper 1. The middle of the first layer is located at about 40 m above the surface and the 15th at about 60 km (the pressure is zero at the top of this layer). As pointed out in paper 1, even a coarse horizontal resolution (the low resolution) is sufficient to reproduce, at least qualitatively, the main features of the available observations of the Martian atmospheric circulation. The low resolution was generally retained for sensitivity studies.

Surface Conditions

In addition to the model parameters, three maps are introduced for the surface conditions: orography, visible albedo, and thermal inertia. These maps correspond to the consortium data set, completed by more recent estimation of the surface thermal inertia and albedo in the polar regions [*Keegan et al.*, 1991; *Paige and Keegan*, 1991], which were provided to us by J. B. Pollack.

4. The Control Simulation

Description

In the present section, we describe a first simulation, which is afterward used as a reference for the sensitivity study. In this "control simulation," the dust visible optical depth is a constant over time and space. Its value is set to 0.2, which corresponds to typical clear-sky conditions [*Martin*, 1986] . Vertically, the dust mixing ratio is almost constant from the surface up to the 0.3-mbar level and then strongly decreases, as proposed by *Pollack et al.* [1990]. The mixing length for vertical turbulent mixing is fixed to 35 m as in the LMD terrestrial GCM. The surface roughness is set to 1 cm everywhere, a value typical of near Viking lander conditions [*Sutton et al.*, 1978] . The emissivity of the bare surface (without ice) is fixed to 0.95, as suggested by *Santee and Crisp* [1993]. The CO_2-ice thermal emissivity ϵ and visible albedo A are set to 0.7 and 0.5, respectively (*Pollack et al.* [1993] have found that those values give reasonable fits to the Viking pressure observations). The dust optical properties are fixed, following *Pollack* [1982], with single-scattering albedo and asymmetry factor in the visible of 0.86 and 0.79, respectively, and a ratio between the absorption efficiency in the thermal infrared Q_{abs}(IR) and extinction efficiency in the visible Q_{ext}(Vis) of 0.2.

As mentioned in paper 1, the interaction between explicitly resolved and unresolved motions is parameterized using an iterated Laplacian acting on the potential temperature and wind components. The operator depends upon one time constant, τ_{diss}, which corresponds to the time of dissipation of the smallest resolved scales. The Laplacian is iterated in order to be more selective in the smaller horizontal scales not acting directly on the large-scale dynamics. Here, the number of iterations n_{diss} is fixed to 2, and τ_{diss} is set to 20,000 s between the surface and the 0.1-mbar level, with rapid decrease to $\tau_{\mathrm{diss}} = 10,000$ s above. With such values (which were tuned in order to ensure model stability), the characteristic timescale for the parameterized horizontal dissipation is of the order of 0.2 sol for zonal wave numbers $n \sim 12$, of a few sols for $n \sim 6$, and of more than a few tens of sols for $n \leq 3$.

The initial state was taken from an old simulation and, after a phase of stabilization (shorter than one Martian year) due to the modification of model parameters, we simulated 5 consecutive Martian years in order to estimate the interannual variability of the model results, which is of course, crucial for sensitivity studies. For comparison with Viking observations, the simulated surface pressure is interpolated at the two Viking sites from the four closest grid points. The Viking 1 point is somewhat shifted in longitude (from 47.9W to 42.5W) in order to match the currently assumed altitude of the landing site, 1.5 km below the reference altitude of Mars. For Viking 2 (which is generally assumed to be 1 km below Viking 1), since none of the the four closest grid points is below -2 km, the surface pressure is extrapolated downward based on the hydrostatic relationship using the near surface simulated air temperature. As for the Viking observations, the surface pressures are afterward decomposed in terms of seasonal variations and transient eddies. For the seasonal evolution, instead of comparing directly the observed and simulated pressure at the two Viking sites, we present on the one hand, direct comparisons for the Viking 1 site only and use, on the other, the relative pressure difference between Viking 2 and 1 in order to compare the observed and simulated meteorological component.

Viking 1 Pressure

The eight-harmonic fit to the simulated pressure at Viking 1 is reported in Figure 5 (thin solid curves). The interannual variability of the simulated seasonal pressure variations appears to be very weak. The amplitude of the seasonal variations is comparable to Viking 1 observations (dashed curve). This amplitude was some-

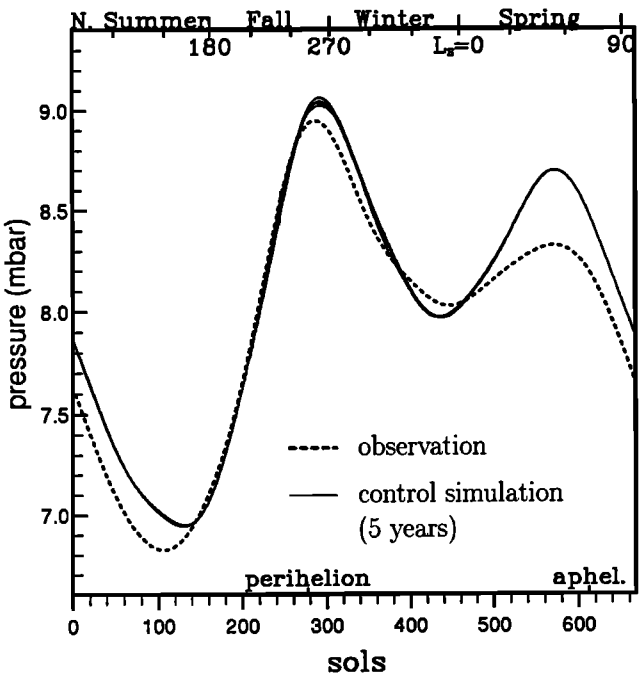

Figure 5. Eight-harmonic L_S fits to the seasonal evolution of the surface pressure at Viking 1. The thin solid curves, almost superimposed, correspond to the five consecutive years of the control simulation. The thick dashed curve (shown in Figure 1) corresponds to Viking 1 observations.

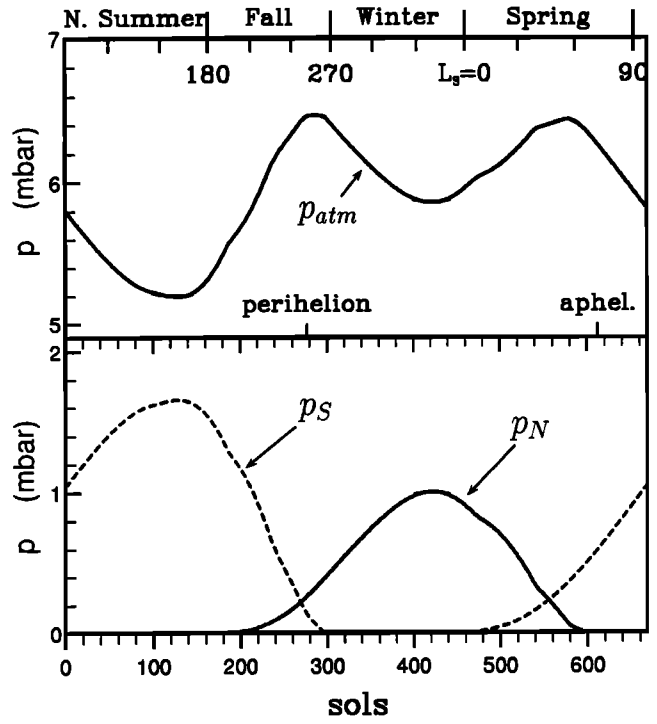

Figure 6. Time evolution of the mean atmospheric surface pressure p_{atm} (upper panel) and that of the equivalent surface pressure of the northern (p_N) and southern cap (p_S) for the first year of the control simulation. The sum of the three components p_{tot} (not shown) does not evolve along seasons and is equal to 6.854 mbar for the control experiment.

what overestimated in the simulations of paper 1. The difference is mainly due to the change of the albedo and emissivity of the polar ice, whereas the introduction of the diurnal cycle (which was tested independently) appears to have a minor effect on the seasonal pressure variations. In the present simulation, the minima and maxima occur approximately at the right seasons. However, a significant discrepancy exists between observations and model, the second pressure maximum being too high in the simulation. The amplitude of the second harmonic is also too large if compared to that of the first harmonic (compare Table 2 for the simulated pressure with Table 1) resulting from an insufficient asymmetry between the two hemispheres.

Planetary Mean of the Surface Pressure

The planetary mean of the surface pressure, p_{atm}, is shown in Figure 6 for the first year of the control simulation, as well as the equivalent pressure of the CO_2 trapped in each cap, p_N and p_S. First, it must be noticed that there is no permanent polar cap in our numerical experiments (this is a common point of most numerical studies of the atmospheric mass budget on Mars). Since the maximum mass of a given cap coincides with a bare pole in the other hemisphere, each pressure minimum really coincides with the maximum mass of the winter cap. The pressure maxima correspond to periods where the two caps are present but very small. The interannual variability of those three curves is very weak and would not be visible on the graph. Thus the small variability in the Viking 1 pressure (Figure 5) is caused almost exclusively by changes in the internal mass redistribution (meteorological component).

Table 2. Phase Lag (Solar Longitude of the Maximum Pressure) and Amplitude of the First Two Harmonics of the Pressure Seasonal Cycle as Simulated at Viking 1 for the First Year of the Control Simulation

Mode k	$p^{(k)}$, mbar	$L_S^{(k)}$, deg
0	8.063	
1	0.613	320.19
2	0.628	69.87

Relative Pressure at the Two Sites and Interannual Variability

Figure 7 shows the simulated relative pressure difference between the two landing sites for the five years. The amplitude is in good agreement with Viking observations with a maximum near northern winter solstice and a minimum at southern winter solstice, but high-frequency variations are weaker in the simulation.

The simulation shows year–to–year variability but smaller than the discrepancy from Viking data. These interannual variations are due to modifications in the global latitudinal pressure variations. We will concen-

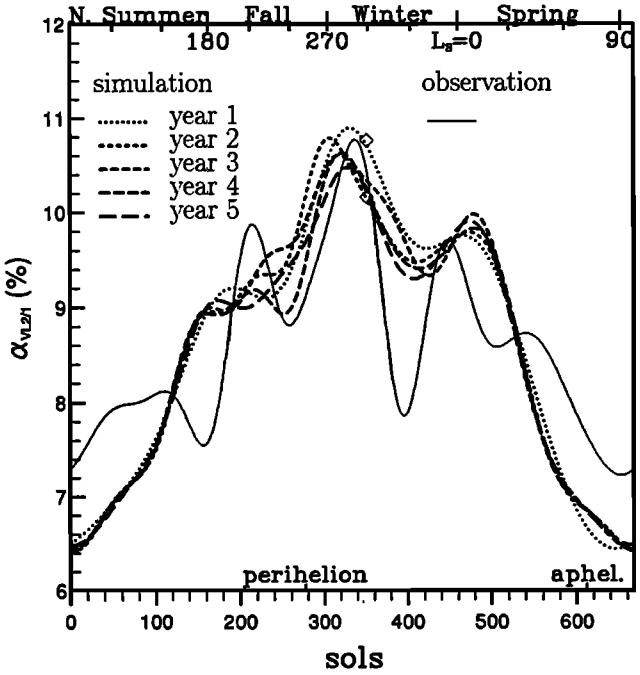

Figure 7. The relative pressure difference between Viking 2 and Viking 1. The thin solid curve (shown in Figure 3) is the observation, and the thick curves correspond to the five successive years of the control simulation.

trate our analysis on the difference between the first and second year of the simulation at $L_S \sim 300$. The corresponding values of $\alpha_{VL2/1}$ have been marked with diamonds in Figure 7. Relative to the Viking 1 pressure, the Viking 2 pressure is about 0.55% lower in the second year. This is directly related to a change in the zonal wind shown in Figure 8. The upper panel shows the mean zonal wind for the first two years for $L_S = 295$ to 305. We recognize (1) the strong eastward jet in the northern middle and high latitude in geostrophic balance with the strong latitudinal gradient at the edge of the polar cap; (2) the near-surface eastward jet in the southern tropics created, as the Indian monsoon winds on Earth, by transport of angular momentum across the equator in the lower branch of the Hadley cell; and (3) rather weak winds in the rest of the southern hemisphere. The difference between year 1 and year 2 (lower panel) can be interpreted as an equatorward displacement of the winter jet.

The wind in the third layer of the GCM ($p/p_s = 0.966$ and $z \sim 300$ m) is shown for the two years in the upper panel of Figure 9 and the latitudinal pressure variation corresponding to geostrophic balance with this near surface zonal wind is reported in the middle panel of the same figure. The relative difference between year 1 and year 2 of that dynamical component is the solid curve of

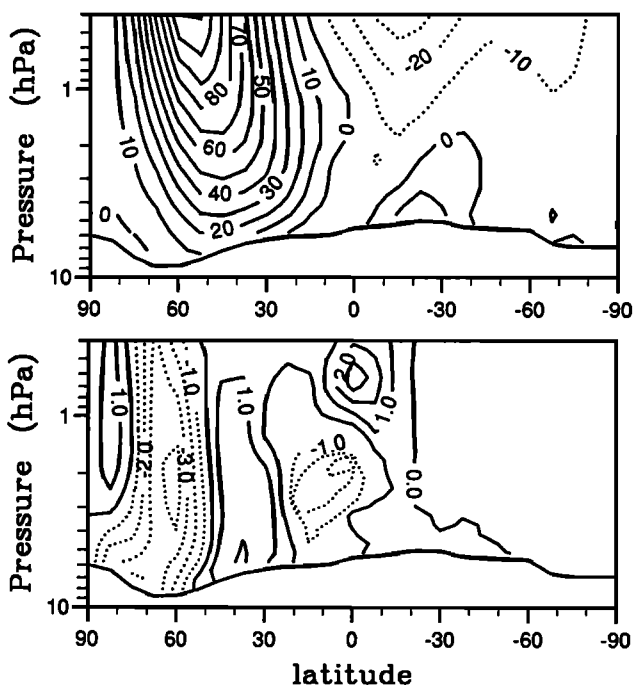

Figure 8. Zonally averaged zonal wind (m s^{-1}) in the control experiment, just after northern solstice (L_S = 295 to 305). The upper panel shows the mean zonal wind for the first two years of the simulation, and the lower panel the difference between year 1 and 2 (year 2 − year 1).

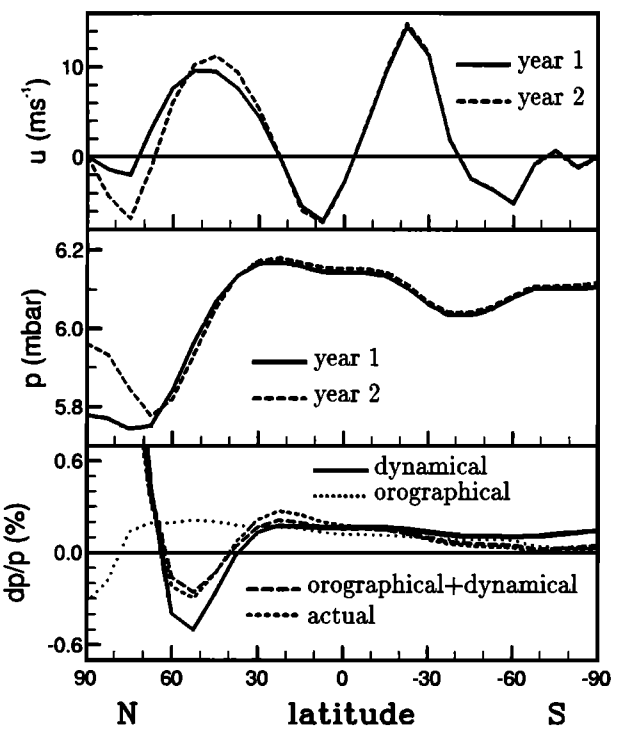

Figure 9. Diagnostic of the pressure differences between year 1 and year 2 of the control simulation (see paper 1 for details). **(Upper panel)** Zonally averaged zonal wind in the third atmospheric layer ($p/p_s = 0.966$ and $z \sim 300$ m) for the first two years. **(Middle panel)** Latitudinal pressure profiles in geostrophic balance with the zonal winds of the upper panel. **(Lower panel)** Various contributions to the pressure modification between year 1 and 2 (percent): dynamical (computed as the relative difference between the two curves of the middle panel) and orographical contributions and their combined effect (computed as the sum of the latitudinal derivative of the two contributions) as well as the actual pressure change.

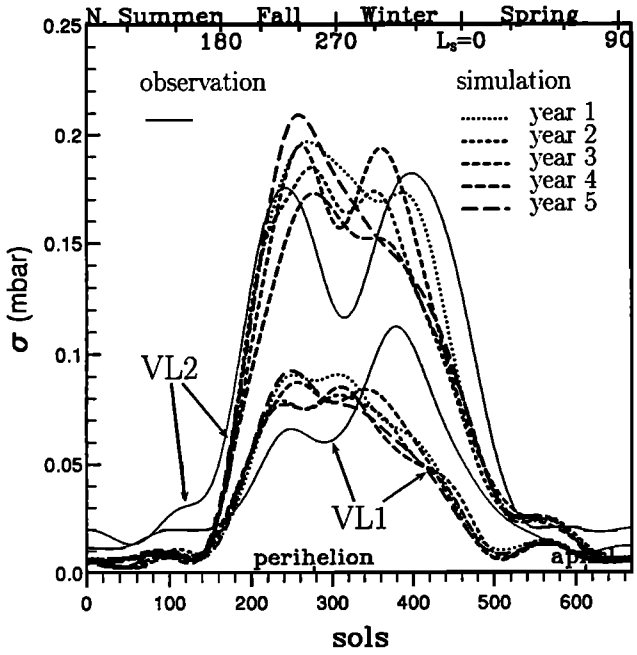

Figure 10. Amplitude of the transient pressure variations at Viking sites. The thin solid curve (shown in Figure 4) is the observation, and the thick curves correspond to the five successive years of the control simulation.

the lower panel. The corresponding pressure changes at Viking latitudes (22N for Viking 1 and 48N for Viking 2) are compatible with the change in the pressure simulated at Viking sites, which means that these pressure changes are almost totally explained by the modification of the mean zonal winds. Note also the good agreement between the actually simulated pressure modification and that reconstructed from the orographical and dynamical contributions.

Transients

Finally, the seasonal evolution of the amplitude of the simulated transient eddies is compared to Viking data in Figure 10. The agreement with Viking data is rather good in view of the very coarse horizontal resolution of this simulation. This is probably the consequence of the importance of transient waves with small wave numbers, which can be well simulated, even with such a coarse resolution. Once again, there is an interannual variability, but less than the discrepancy with observations. The model does not simulate the decrease of the amplitude of the transient eddies near northern winter solstice, and the decrease of this amplitude at the end of the northern winter is somewhat anticipated.

5. Sensitivity to Model Parameters for Clear-Sky Conditions

We present a series of numerical experiments performed by changing some model parameters, starting at $L_S = 330^o$ (from a state of the control simulation) just before the formation of the southern polar cap in order to minimize the memory of the climatic system. In all the simulations the northern cap disappears near $L_S = 90$, after which the seasonal mass cycle adjusts in the sense that the total atmospheric mass is almost unchanged after one more year of simulation. Each sensitivity experiment thus includes an adjusting period going from $L_S = 330^o$ to $L_S = 98^o$ (date of the Viking 1 landing) followed by a 1-year simulation used for comparisons with the control simulation and Viking observations.

In this first set of experiments, the dust optical depth is kept to its "clear-sky" value: $\tau = 0.2$.

Horizontal Resolution

A simulation was performed at high horizontal resolution (64 longitude points and 48 latitude points) using exactly the same set of parameters as for the control simulation except for the near-surface horizontal diffusion time constant, which was set to $\tau_{\text{diss}} = 12,000$ s. This corresponds to a horizontal dissipation about 8 times weaker than that of the control simulation at a given spatial scale.

The seasonal variations of the surface pressure are compared to the control experiment and to the observations in Figure 11. In terms of the Viking 1 seasonal pressure variations, a simple quadratic error analysis would suggest that the agreement with observations is worse with the high resolution. However, it must be kept in mind that the total CO_2 mass is an adjustable parameter which directly influences the mean value of the simulated pressure. In fact, the results are somewhat better for the high resolution, since the differ-

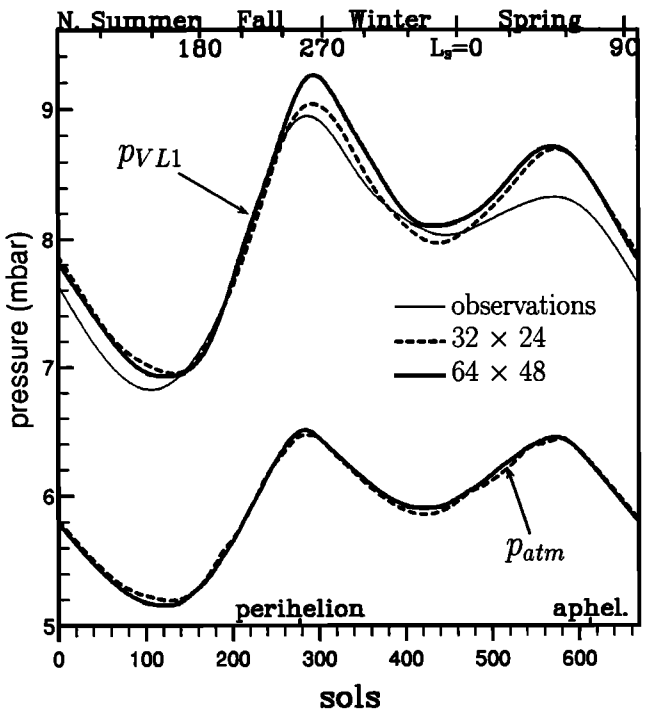

Figure 11. Viking 1 pressure, p_{VL1}, as simulated with the low (32 longitude points and 24 latitude points) and high (64 longitude points and 48 latitude points) horizontal resolutions, Viking observations and the simulated mean atmospheric pressure, p_{atm}.

ence between the two pressure maxima is somewhat enhanced. The change does not come from the atmospheric mass budget, which is almost unmodified (see the lower curves in Figure 11), but from the meteorological contribution α_{VL1}. The representation of the differential pressure between Viking 1 and 2 is also closer to observations as shown in Figure 12, with a better amplitude and stronger rapid oscillations (Figure 7) than for the low resolution. However, the improvement of the amplitude must be taken rather carefully: it can be the consequence of changes in the representation of the winds but also of the modification of the representation of the orography at Viking sites.

For transient eddies (Figure 13), the main improvement, with respect to the control simulation (see Figure 10), is their longer persistence during late winter. Note that the main discrepancy with Viking observations is an overestimation of the amplitude of the transients near northern winter solstice.

In all the sensitivity experiments performed herein, we use the low horizontal resolution (in order to be able to perform a large number of experiments at a reasonable numerical cost), although a finer horizontal resolution would have been preferable to correctly represent the atmospheric dynamics.

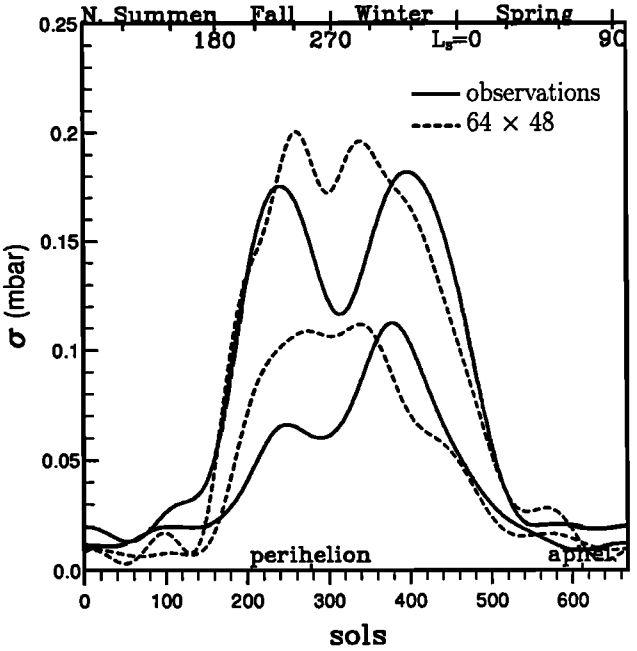

Figure 13. Amplitude of the transient pressure variations at Viking sites computed from observations and from the results of the high-resolution simulation (64 longitude points and 48 latitude points).

Surface Roughness

Sutton et al. [1978] deduced values of 0.1-1 cm for the surface roughness length, based on the camera images of the surface around the Viking landers. These values, which were derived for local studies of the planetary boundary layer, are not representative of a mean Martian surface and may also not be appropriate for GCM's. It must be noted that even for terrestrial GCM's, a good determination of the roughness length is an open question. At the same time, this surface roughness strongly influences the near-surface wind and, in turn, the dynamical component of the horizontal pressure variations. Some recent experiments performed with the LMD terrestrial climate GCM, have shown, for instance, that a decrease by a factor of 2 of the surface drag coefficient leads to latitudinal pressure gradients 25% steeper in the southern midlatitudes (30-60S), where because of the absence of a significant orography, the horizontal pressure variations are completely dominated by the geostrophic balance with near-surface winds (dynamical component).

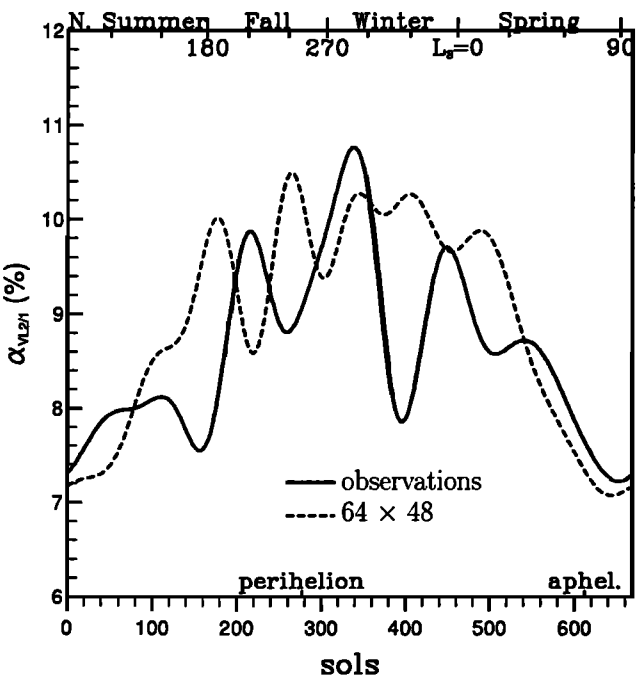

Figure 12. The $\alpha_{VL2/1}$ computed from observations and from the results of the high-resolution simulation (64 longitude points and 48 latitude points).

Four simulations were conducted for z_0 = 0.1 mm, 1 mm, 10 cm and 1 m (the control value was 1 cm). The simulated atmospheric pressure p_{atm} is almost identical for the five experiments (including control), but there is significant effect on the relative pressure difference between Viking 2 and 1 (Figure 14): for the period L_S = 300 to 307, for instance, $\alpha_{VL2/1}$ = 9.7% for z_0 = 1 mm and $\alpha_{VL2/1}$ = 10.7% for z_0 = 10 cm (diamonds in Figure 14). As for the interannual variations of the control experiment, the local pressure changes at Viking sites are representative of the modification of the zonally averaged surface pressure (a 0.5% decrease at 22N and a 0.6% increase at 48N, lower panel of Figure 15) and are a direct consequence of the reduction of the intensity of the near-surface zonal wind (upper panel). Note that the change does not affect significantly (in comparison to the interannual variations) the global zonal wind distribution, but selectively, the near-surface winds. It is also noticeable that such large

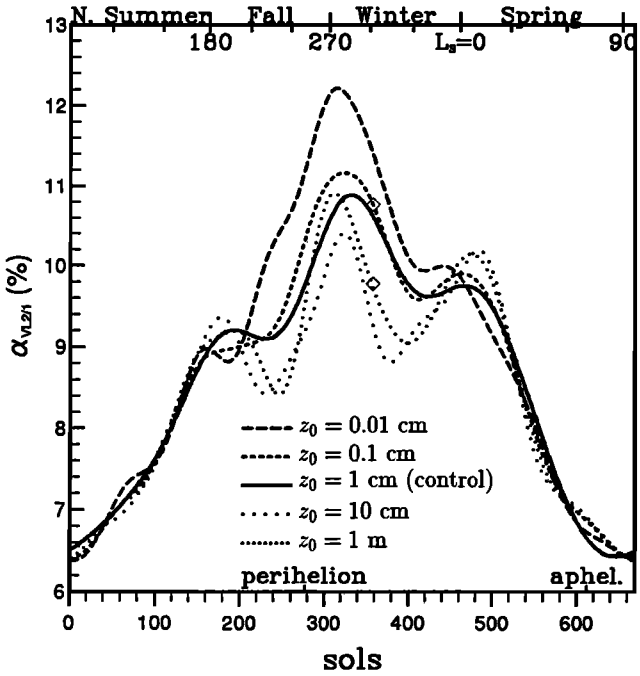

Figure 14. Relative meteorological factor between Viking 2 and 1 for various values of the surface roughness length z_0. The two diamonds (from the $z_0 = 0.1$ cm and $z_0 = 10$ cm experiments) are analyzed in detail in the text.

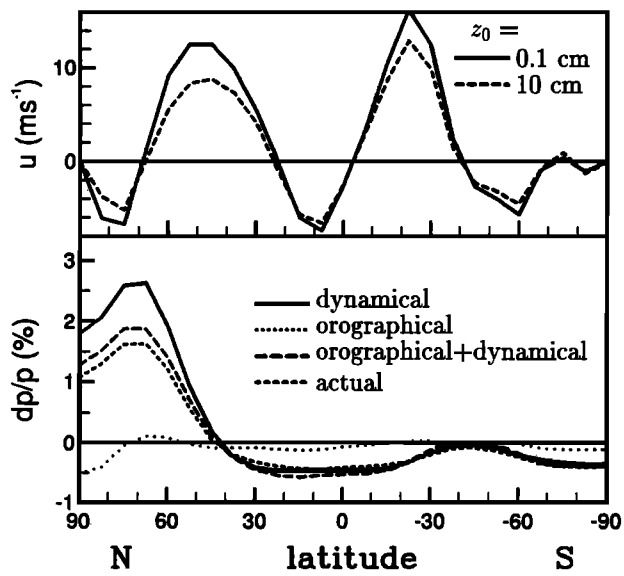

Figure 15. (Upper panel) Mean zonal wind (m s^{-1}) in the third atmospheric layer ($p/p_s = 0.966$ and $z \sim 300$ m) for the $z_0 = 0.1$ cm and $z_0 = 10$ cm sensitivity experiments for the period $L_S = 295 - 305$. **(Lower panel)** Various contributions to the pressure modification between $z_0 = 0.1$ cm and $z_0 = 10$ cm (percent): dynamical and orographical contributions and their combined effect (computed as the sum of the latitudinal derivative of the two contributions) as well as the actual pressure change.

changes in the surface drag do not affect significantly the amplitude of the transient pressure variations (not shown).

Caps Albedo and Emissivity

Four experiments were performed by changing the ice visible albedo A or thermal emissivity ϵ simultaneously on the two caps. The four experiments correspond to $A = 0.4$, $A = 0.6$, $\epsilon = 0.6$, and $\epsilon = 0.8$. Albedo and emissivity have a direct impact on the energy budget on the caps and therefore strongly affect the mass budget. This is illustrated in Figure 16 and Figure 17, which show the time evolution of the equivalent pressure of the two caps. As expected, a reduction of the ice albedo (Figure 16) increases the absorption of the solar radiation, and reduces the mass of the polar cap. Emissivity acts in the same direction (Figure 17): less thermal emission by the cap results in smaller polar caps. However, the effect of the change in albedo and that of emissivity are not completely equivalent: a change in the ice emissivity has a rather constant effect during both the formation and recession phase, whereas albedo changes have a much weaker effect during the cap formation which mainly occurs in the polar night.

The dynamical component, $\alpha_{VL2/1}$, and the transient pressure variations are not significantly affected by the modifications of the ice properties.

Other Uncertain Parameters

The choice of the parameters which have been varied involve very different physical processes and may give, all together, an overview of the sensitivity of the simulated atmospheric circulation to the values of the model parameters: the changes of horizontal resolution and dissipation time constants directly influence

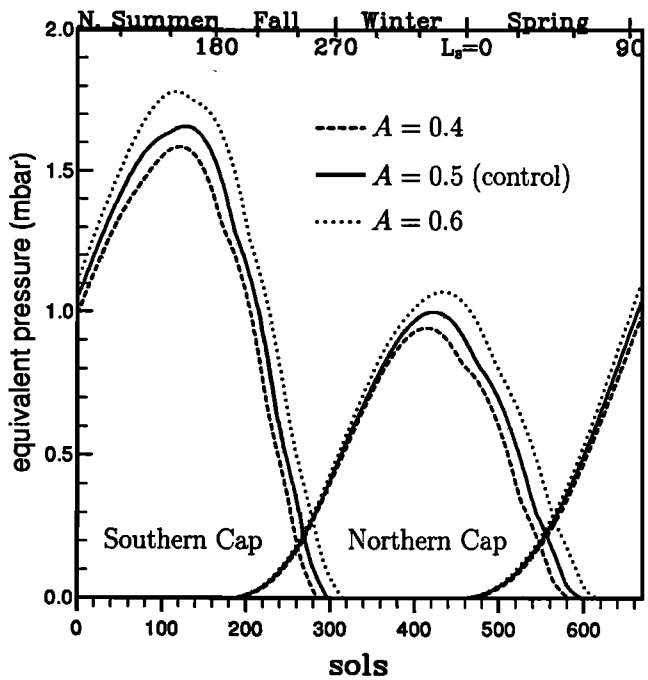

Figure 16. Time evolution of the equivalent pressure of both polar caps for various values of the ice albedo: $A = 0.4$, 0.5 (control), and 0.6.

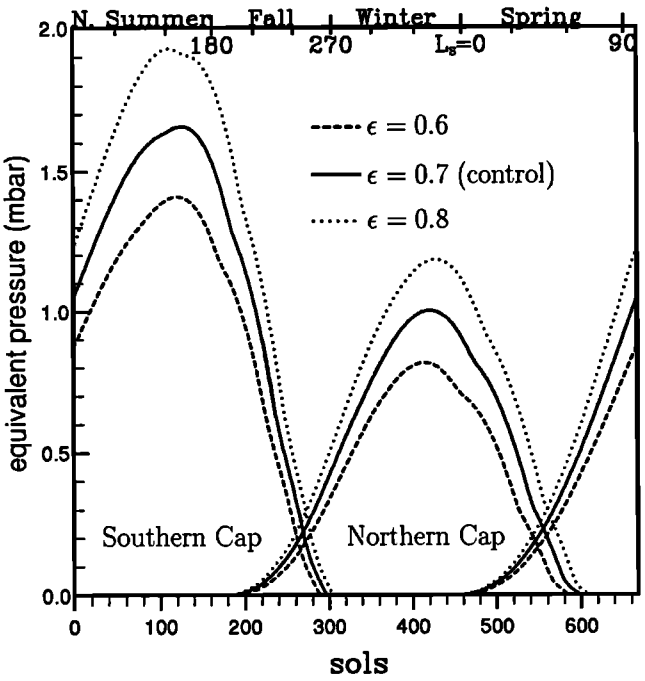

Figure 17. Time evolution of the equivalent pressure of both polar caps for various values of the ice emissivity: $\epsilon = 0.6$, 0.7 (control), and 0.8.

the global atmospheric dynamics and, in particular, the representation of the transient and stationary eddies; the surface roughness has a rather selective impact on the meteorological pressure variations, not affecting significantly the general dynamics and energy and mass budget, whereas the emissivity and albedo changes selectively affect the energy and mass balance of the polar regions. However, some other very uncertain parameters can significantly influence our results. *Wood and Paige* [1992] have shown, for instance, that the seasonal pressure variations, simulated with an energy balance model, are very sensitive to the soil thermal inertia. The thermal inertia we use [*Keegan et al.*, 1991; *Paige and Keegan*, 1991] corresponds to the skin surface and may not be adapted for seasonal variations. The Martian orography is also rather poorly known. It has a direct influence on the meteorological contribution as well as on the emissivity of the polar caps since their temperature is directly related to the surface pressure through the solid-vapor pressure curve.

6. Dusty Conditions

Another series of sensitivity experiments was performed for different values of the dust opacity.

Dust optical depths show a very large spatial and temporal variability on Mars, large enough to significantly affect the atmospheric energy and mass budget [e.g., *Pollack et al.*, 1990, 1993]. Unfortunately, there is no complete climatology of the Martian dust optical depth, at least for a year without great dust storms, which could be used to constrain numerical simulations (the best temporal coverage corresponds to the Viking infrared thermal mapper (IRTM) data analyzed by *Martin and Richardson* [1993]). In this section, we first present simple sensitivity experiments performed with various values of the global dust optical depth: $\tau = 0.2$, 0.5, 1, and 2.5. A stronger horizontal dissipation in the upper atmosphere was needed for model stability when increasing the dust optical depth, probably due to shorter radiative time constants. For $\tau = 0.2$, 0.5, and 1, we use the same time constant as for the control experiment in the lower atmosphere ($\tau_{\text{diss}} = 20,000$ s), but $\tau_{\text{diss}} = 4000$ s above 0.15 mbar. For $\tau = 2.5$, we set $\tau_{\text{diss}} = 15,000$ s in the lower atmosphere and 2000 s in the upper atmosphere. The $\tau = 0.2$ experiment (same value as for the control experiment) was performed in order to make the three first experiments ($\tau = 0.2$, 0.5, and 1) identical except for the dust optical depth, and to check the impact of changing the horizontal dissipation parameters for the $\tau = 0.2$ case.

Effect on the Mass Cycle

The first effect of an increase of the dust opacity in our model is a global increase of the amount of carbon dioxide trapped in the caps, as shown in Figure 18, somewhat in contradiction with the results obtained by *Pollack et al.* [1990], which showed a small decrease of the condensation rate at $L_S = 279$ for increasing dust optical depths. In fact, the reduction of the atmospheric mass, in our simulations, is mainly due to a reduction of the sublimation rate during cap recession, especially near spring equinox, the formation phase being much less affected. The extension of the caps is also modified (Figure 19): for larger values of τ, the caps are smaller during their formation but larger at the end of the recession.

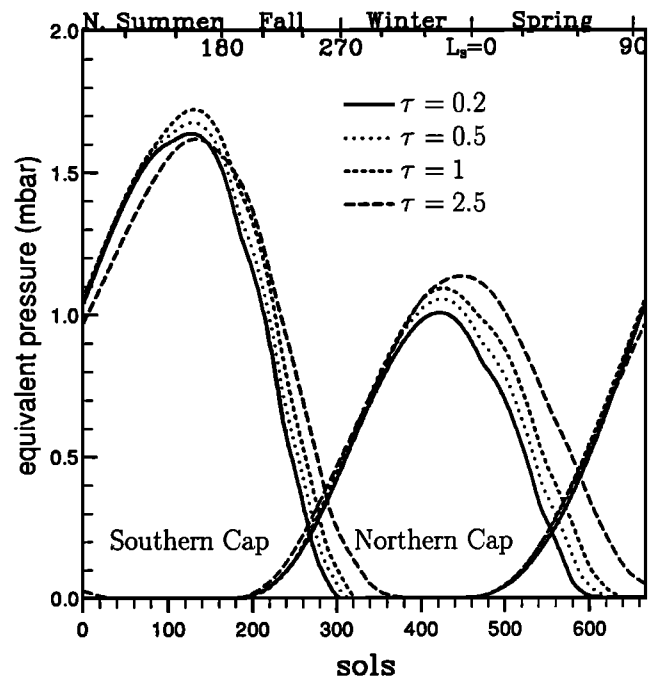

Figure 18. Time evolution of the equivalent polar cap pressures p_N and p_S for the various dust sensitivity experiments ($\tau = 0.2$, 0.5, 1, and 2.5).

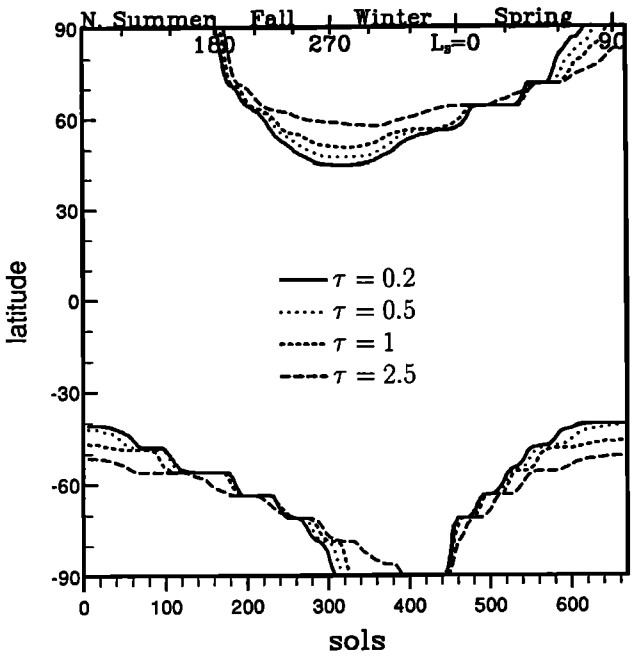

Figure 19. Time evolution of the mean latitude of the edge of the polar caps for the dust sensitivity experiments ($\tau = 0.2$, 0.5, 1, and 2.5).

The sensitivity of the climate to the dust optical depths involves radiative as well as dynamical mechanisms. Here, we center our analyses on the $\tau = 0.2$ and $\tau = 1$ experiments (which are representative of the seasonal variability of dust for years without global dust storm) and on a period just before northern solstice ($L_S = 253 - 259$) when the northern cap is forming while the southern cap is still subliming.

Modifications of the Radiative Budget

The solar radiation (noted SW hereafter) reaching the surface is much smaller in the $\tau = 1$ than in the $\tau = 0.2$ experiment, by about 16% in midlatitude and 40% (40 W m^{-2}) on the southern cap (upper panel in Figure 20; note that the insolation is null from the northern pole down to 67°N during that period). The total planetary albedo is also somewhat reduced in the $\tau = 1$ experiment (see SW$^{\uparrow}$, second panel of Figure 20), the increase of the atmospheric albedo, resulting from dust scattering, being smaller than the reduction of the visible light reflected by the surface, especially on the highly reflecting polar ice. As a result, for $\tau = 1$, more visible radiation is absorbed by the global system (atmosphere plus solid planet), and much more by the atmosphere alone, especially in the summer hemisphere, which increases the latitudinal thermal contrasts.

The surface temperature is almost identical in the two simulations, as can be seen from the surface thermal emission ($\epsilon_s \sigma T_s^4$, Figure 20), which is only significantly affected near the edge of the southern cap due to a larger ice cover in the 70-80S region at that particular season (also responsible for the larger planetary albedo for $\tau = 1$ in this latitude range). The atmospheric thermal radiation absorbed by the surface ϵ_s LW$_s^{\downarrow}$ is larger in the $\tau = 1$ experiment, as expected from the larger atmospheric emissivity. This flux is also affected by the modifications of the atmospheric temperature shown in Figure 21. The atmosphere is globally warmer in the $\tau = 1$ experiment, as a consequence of the larger direct absorption of solar radiation, but colder by about 5 K over the forming cap, up to the 3-mbar level. On the north pole itself, the temperature is not affected and corresponds in both cases to a condensing atmosphere

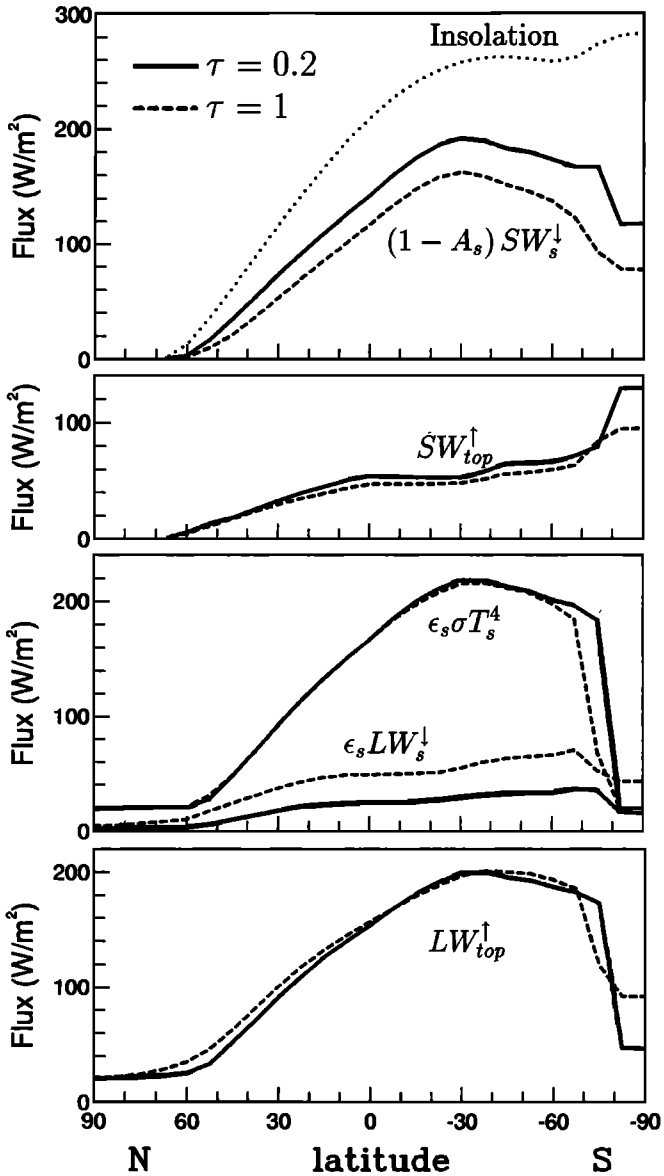

Figure 20. Radiative fluxes at the surface and top of the atmosphere computed for the $\tau = 0.2$ (solid curves) and $\tau = 1$ (dashed curves) sensitivity experiments just before northern winter solstice, $L_S = 253 - 259$. From top to bottom: (1) the insolation at the top of the atmosphere and solar radiation absorbed by the surface; (2) the outgoing shortwave radiation at the top of the atmosphere; (3) the surface thermal emission and the atmospheric thermal radiation absorbed by the surface; (4) the total thermal emission to space.

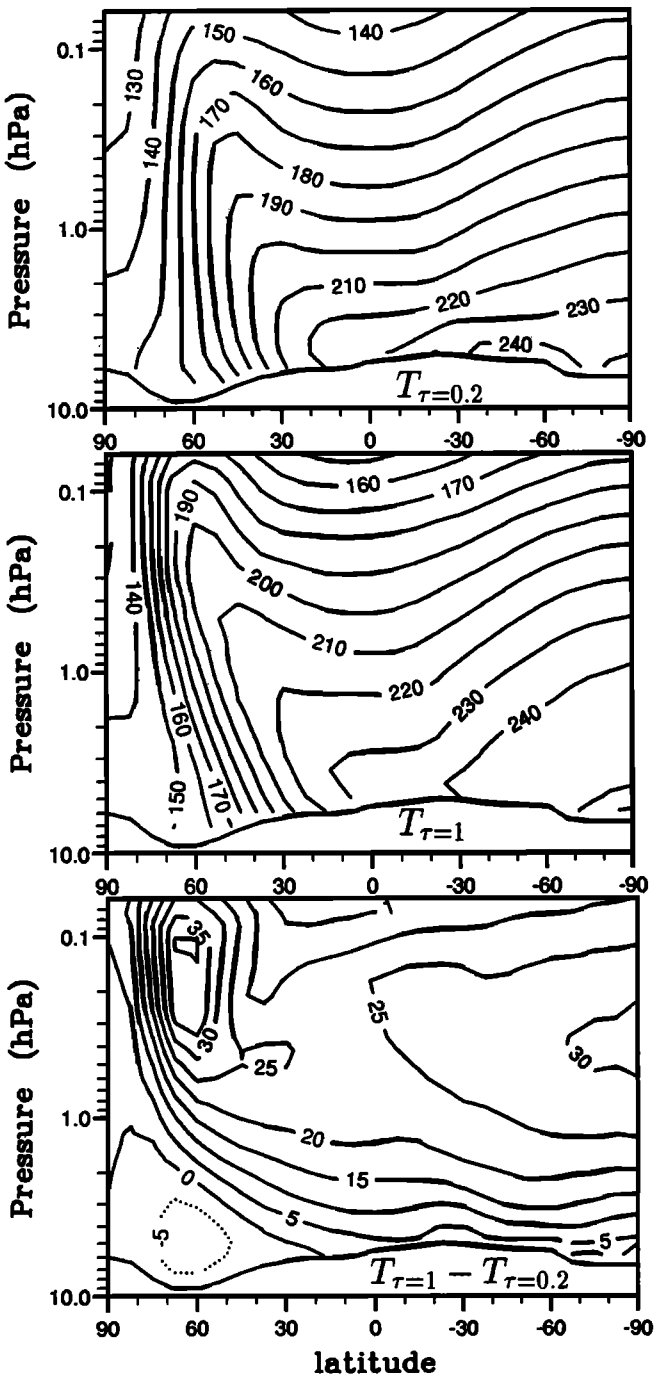

Figure 21. Zonally averaged temperature simulated just before northern winter solstice ($L_S = 253-259$) for the $\tau = 0.2$ (upper panel) and the $\tau = 1$ (middle panel) experiment as well as the difference between both (lower panel).

up to very low pressures. Note that the atmospheric condensation extends to much lower latitudes for the $\tau = 0.2$ than for the $\tau = 1$ simulation (not shown).

On the northern pole surprisingly, although the air temperature decreases with altitude, the thermal emission to space, $LW^{\uparrow}_{top}$, is (1) somewhat larger than the surface thermal emission for both simulations and (2) larger in the $\tau = 1$ than in the $\tau = 0.2$ experiment. Both results are the consequence of the low thermal inertia of the icy surface, which minimizes the role of the emission emitted by the surface and enhances the role of the thermal emission by the atmosphere (in particular through its reflection on the surface) as can be checked with a simple analytical one-layer radiative transfer model.

Note that for a ice emissivity $\epsilon = 1$, *Pollack et al.* [1990] found a decrease of the total condensation rate at this season for increasing dust amounts.

Finally in our simulations, the net effect, in terms of atmospheric radiative budget at the top of the atmosphere, of an increase of τ from 0.2 to 1 are (Figure 22, upper panel): (1) an increase of the hemispheric asymmetry with a larger gain of energy in the summer hemisphere and larger loss in the winter hemisphere (including the polar region); and (2) a decrease of the strong energetic gain on the subliming cap (except at the edge of the cap due to the different cap extensions of the two simulations).

Energy and Mass Budget in the Polar Regions

In fact, there is a great difference between the processes controlling the formation and the recession of the polar caps. During recession, the mass exchange is controlled by the surface heat balance (compare upper and

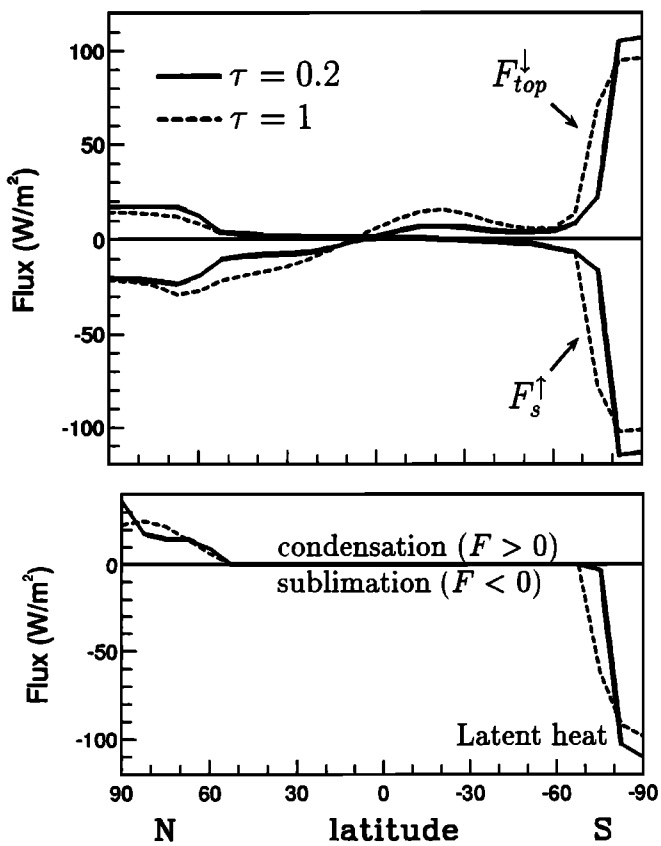

Figure 22. Net radiative fluxes at the top of the atmosphere and at the surface (upper panel, positive for a gain of energy by the atmosphere) and latent heat release (lower panel) computed for the $\tau = 0.2$ (solid curves) and $\tau = 1$ (dashed curves) sensitivity experiments just before northern winter solstice, $L_S = 253 - 259$. The net surface flux includes the turbulent flux.

lower panel of Figure 22) which is itself very close to the radiative balance at the top of the atmosphere, due to the weak role of the thermally driven circulation, shown in the upper panel of Figure 23. To the contrary, during winter, condensation occurs both in the atmosphere and on the surface, and since the radiative fluxes are much smaller, the latitudinal heat advection plays a significant role in the model sensitivity.

What we call thermally driven circulation hereafter is the total circulation minus the condensation flow (second panel of Figure 23). As proposed by *Pollack et al.* [1990], the condensation flow is defined at a given latitude as the zonally and vertically averaged meridional mass flux. The condensation flow accounts for the latitudinal mass redistribution and includes, in fact, in addition to condensation, the meteorological latitudinal mass redistribution. On the subliming cap, the condensation flow is the principal component of the latitudinal energy transport and just corresponds to the transport toward lower latitudes of the energy the atmosphere has gained by increasing its mass.

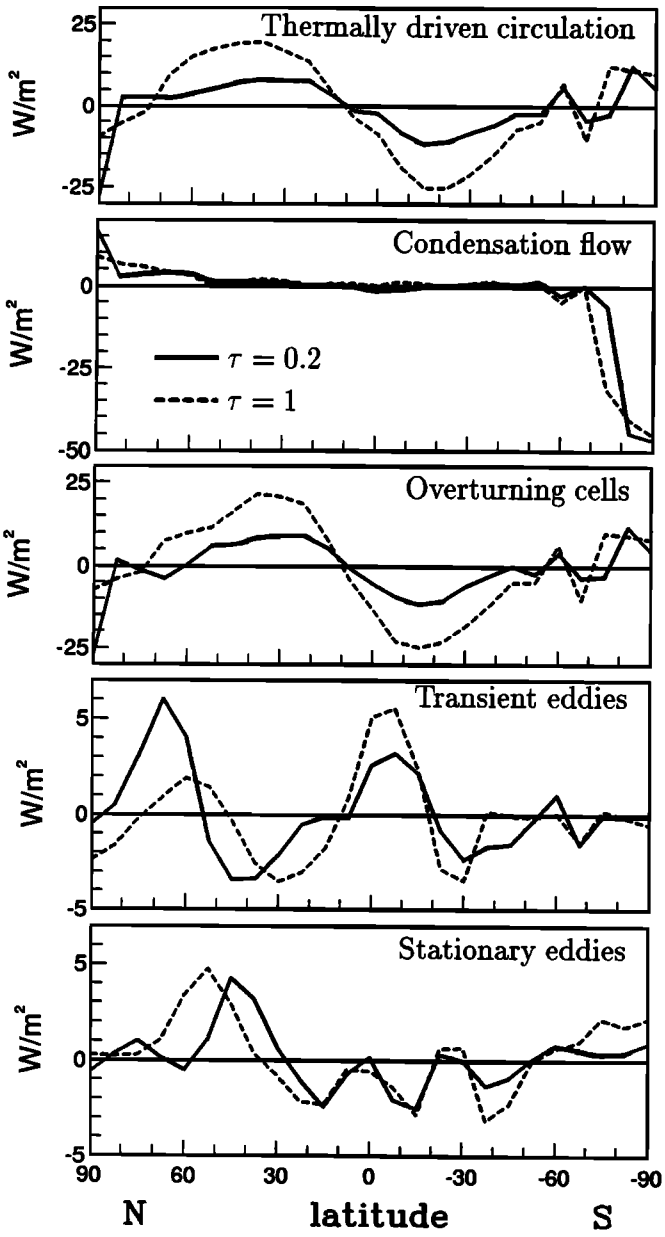

Figure 23. Atmospheric heating (in W m^{-2}) computed for various components of the atmospheric circulation and the $\tau = 0.2$ (solid curves) and $\tau = 1$ (dashed curves) sensitivity experiments just before northern winter solstice, $L_S = 253 - 259$. The thermally driven circulation is the difference of the total circulation and condensation flow. The overturning cell is the difference between the mean meridional circulation and condensation flow.

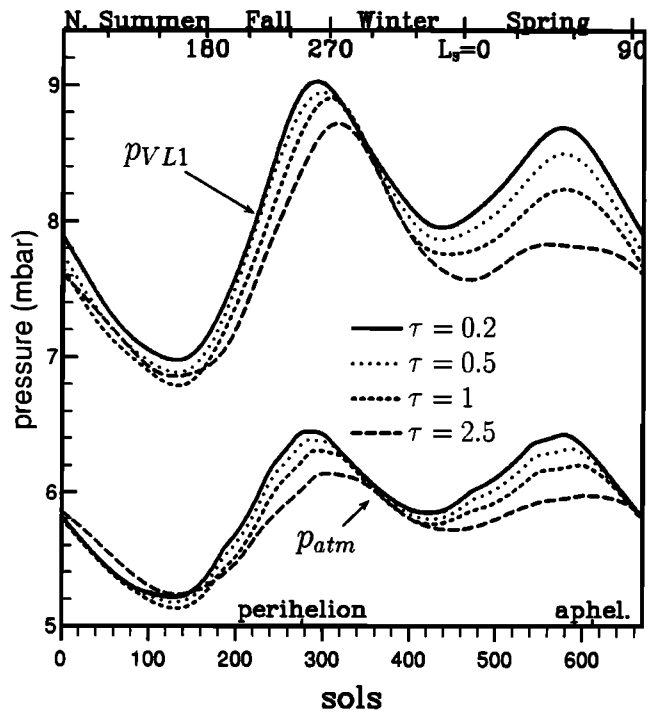

Figure 24. Simulated Viking 1 pressure and planetary averaged surface pressure p_{atm} for the dust sensitivity experiments ($\tau = 0.2$, 0.5, 1, and 2.5).

The cap recession is thus essentially controlled by the radiative balance, giving a simple explanation for the major difference between the $\tau = 0.2$ and $\tau = 1$ simulations. In late winter, when the latitudinal extension of the winter cap is maximum and the sublimation rate is already high in the midlatitudes, the smaller incident flux on the surface plus smaller extent of the cap in the $\tau = 1$ simulation explains the much slower cap recession at this season. Since the recession is slower, the cap finally becomes larger than in the $\tau = 0.2$ case, after which the smaller radiative flux in the $\tau = 1$ experiment is partially compensated by the larger surface of sublimation and leads to almost identical recession rates, in terms of mass, in late spring.

During the cap formation, the slightly larger atmospheric thermal emission to space in the $\tau = 1$ experiment tends to reduce the total (atmosphere plus surface) condensation. Heat advection by overturning cells (mean meridional circulation minus condensation flow) is much stronger in midlatitudes than for the $\tau = 0.2$ simulation, while the transient eddies, which transport energy from middle to high latitudes in the winter hemi-

sphere (as expected from baroclinic eddies), are strongly reduced.

The increased heating by the mean meridional circulation is mainly sensitive near the edge of the cap (50-70N) responsible for a weaker condensation in that region for $\tau = 1$ (lower panel of Figure 22) and for the smaller cap extension during the formation phase (Figure 19). To the contrary, the reduction of the poleward energy transport by transient eddies has a major impact in very high latitudes (70-85N), where it is responsible for a larger condensation rate in the $\tau = 1$ experiment. As a consequence, the mass of the cap is more concentrated near the pole in the $\tau = 1$ experiment.

Seasonal Pressure Variations

The change in the condensation-sublimation affects directly the mean atmospheric pressure p_{atm} (lower curves in Figure 24). For increasing dust opacities, the Viking 1 pressures (upper curves) are closer to observations, in that the second pressure maximum is more reduced than the first one. This is due in part to the modification of the meteorological component α_{VL1} shown in Figure 25. It must be noticed however, that α_{VL1} is mainly sensitive to the dust optical depth near northern summer solstice, which is in reality, the period of minimum atmospheric dust content [*Martin*, 1986] .

The effect on the differential pressure between Viking 2 and 1 (Figure 26) is very different, in that it is large only during northern autumn and winter. It corresponds to a strong increase of the Viking 2 pressure for increasing dust opacities. As for the control and roughness sensitivity experiments, the modification of $\alpha_{VL2/1}$ (by about 2% for $L_S = 295 - 300$) is representative of the modification of the zonally averaged surface pressure (see Figure 27): the main effect is a strong pressure

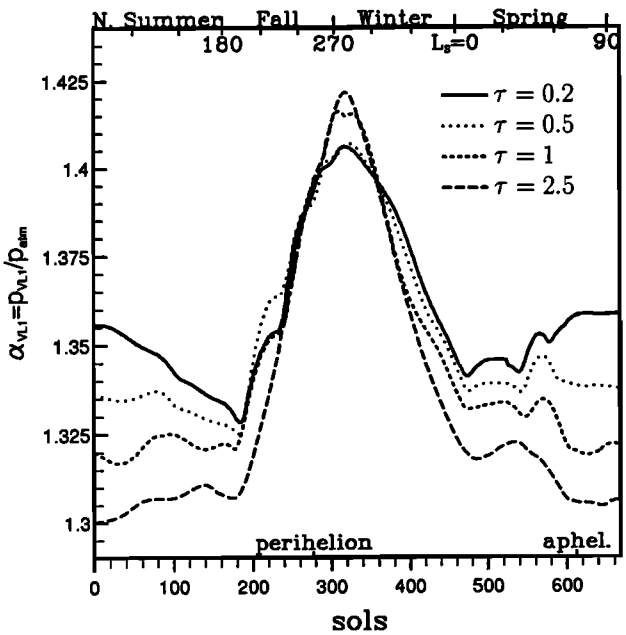

Figure 25. The $\alpha_{VL1} = p_{VL1}/p_{atm}$ for the dust sensitivity experiments ($\tau = 0.2$, 0.5, 1, and 2.5).

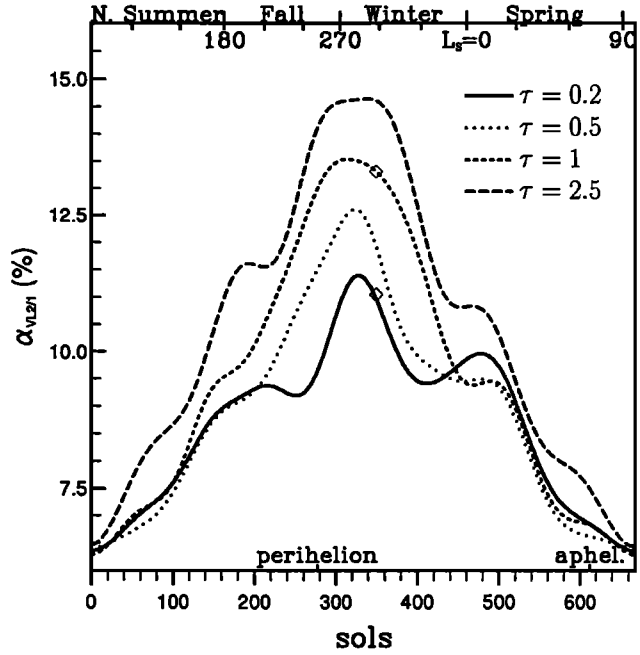

Figure 26. Relative pressure difference $\alpha_{VL2/1}$ between the two Viking sites for the dust sensitivity experiments ($\tau = 0.2$, 0.5, 1, and 2.5).

increase in the northern middle and high latitudes (by about 4% at 60N), corresponding to a weakening of the circumpolar depression due to the reduction of the near-surface eastward winds in the 30N-60N region. In the present case, modifications of the near-surface winds

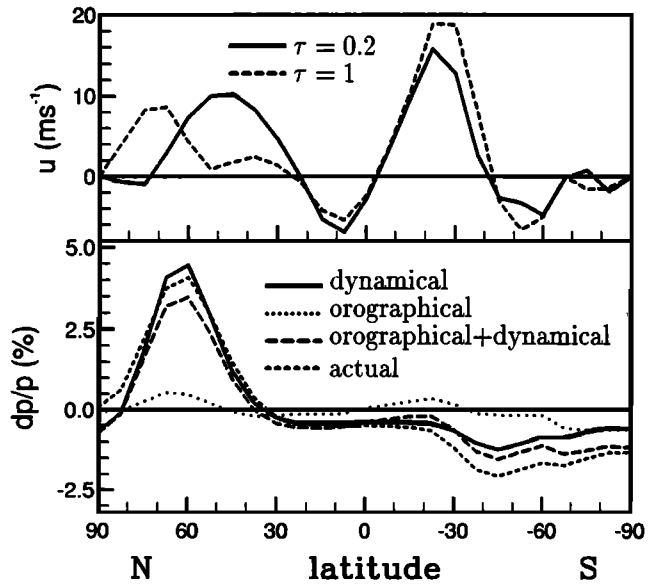

Figure 27. **(Upper panel)** Mean zonal wind (m s^{-1}) in the third atmospheric layer ($p/p_s = 0.966$ and $z \sim 300$ m) for the $\tau = 0.2$ and $\tau = 1$ experiments for the period $L_S = 295 - 300$. **(Lower panel)** Various contributions to the pressure modification between $\tau = 0.2$ and $\tau = 1$ (percent): dynamical and orographical contributions and their combined effect (computed as the sum of the latitudinal derivative of the two contributions) as well as the actual pressure change.

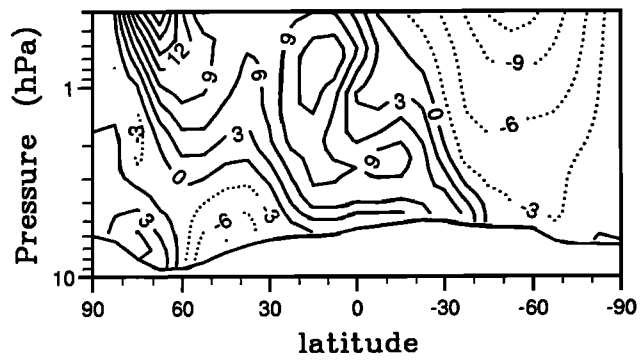

Figure 28. Zonal wind (m s^{-1}) modifications resulting from an increase of the dust visible optical depth from $\tau = 0.2$ to $\tau = 1$ ($L_S = 285$ to 300).

are the signature of large changes in the global wind structure (Figure 28) mainly due to an increase of the mean meridional advection of angular momentum (not shown).

Transient Eddies

The modification of the amplitude of the transient eddies (reported in Figure 29 for Viking 2) is also very instructive. First, the amplitude for the $\tau = 0.2$ experiment is in the range of the variability of the control simulation despite the stronger horizontal dissipation in the upper atmosphere. Note also the general but not systematic decrease of the amplitude of the transients for increasing optical depths, coinciding with the decrease of the latitudinal energy transport mentioned previously. More remarkable is the fact that the reduction is much more effective near northern winter solstice. This result may explain both (1) the two-peak structure found in the amplitude of the transient eddies for the Viking observations (the northern winter solstice corresponding to the maximum dust optical depth both for year with and without global dust storms) and (2) the fact that the amplitude of the transient eddies was much less reduced during the first global dust storm 1977-A, $L_S \sim 210 - 230$, than during the 1977-B dust storm, $L_S \sim 280 - 300$. Note also that the variance of the transient pressure variations in the $\tau = 2.5$ experiment for the period $L_S = 280 - 300$ (about 0.03-0.04 mbar) is of the order of that observed by Viking 2 during the 1977-B dust storm. The explanation for this seasonal behavior would require much more sophisticated diagnostics and is beyond the scope of the present paper, but it is worthwhile noticing that Martian GCM's seem to be well suited for further studies of the Martian transients (see *Barnes* [1980, 1981], and *Barnes et al.* [1993] for more complete studies).

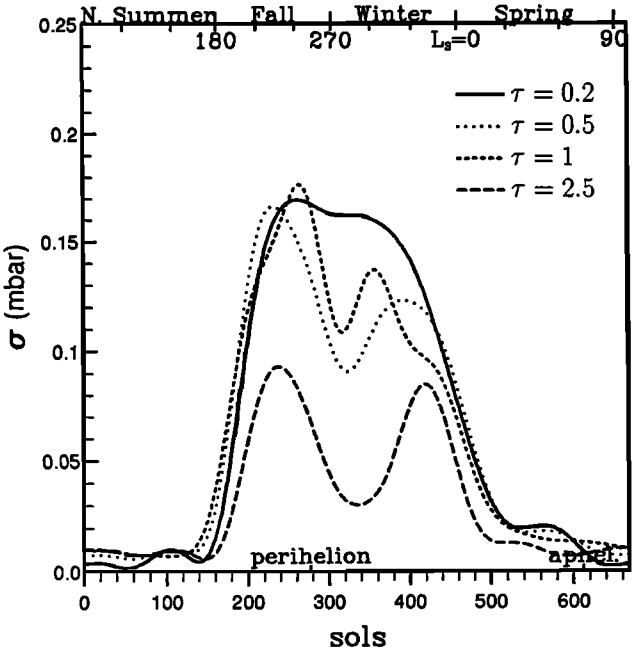

Figure 29. Amplitude of the transient eddies at Viking 2 for the dust sensitivity experiments ($\tau = 0.2$, 0.5, 1, and 2.5).

Time-Varying Dust Opacity

We also performed a sensitivity experiment varying the dust opacity as a simple cosine function of solar longitude ($\tau = 0.6 + 0.3\cos(L_S - L_{S0})$, with $L_{S0} = 280$), which qualitatively matches the seasonal evolution deduced for the Viking years, except for the period of dust storms [*Pollack*, 1982; *Martin*, 1986] .

This experiment is compared to the previous experiments for constant optical depths, in terms of the two first harmonics of the pressure simulated at Viking 1 (Table 3). The improvement of the simulation with increasing optical depth (described previously) is very clear in the two-harmonic decomposition: as τ increases, the ratio between the first and second harmonic increases. The experiment with variable optical depth (VAR1) does not show any significant improvement, even when compared to the $\tau = 0.2$ experiment.

Uncertainties Arising From Dust Optical Properties

Some of the results presented above are rather sensitive to the numerical values adopted for the dust optical properties. In particular, we use in the present paper a ratio $Q_{abs}(IR)/Q_{ext}(Vis)$ of 0.2 taken from *Pollack* [1982], whereas the radiative code of the Ames GCM, which accounts for scattering in the thermal infrared,

Table 3. Phase Lag (Solar Longitude of the Maximum Pressure) and Amplitude of the First Harmonics of the Pressure Seasonal Cycle as Simulated at Viking 1 for the Various Dust Sensitivity Experiments

Experiment	$p^{(0)}$, mbar	$p^{(1)}$, mbar	$L_S^{(1)}$, deg	$p^{(2)}$, mbar	$L_S^{(2)}$, deg
$\tau = 0.2$	8.067	0.592	320.36	0.623	69.99
$\tau = 0.5$	7.965	0.610	316.05	0.602	71.21
$\tau = 1$	7.841	0.626	313.34	0.573	75.10
$\tau = 2.5$	7.703	0.636	311.49	0.506	82.64
VAR1	7.968	0.586	314.22	0.621	73.10
VAR2	7.924	0.601	314.75	0.624	75.14

corresponds to a significantly higher value (J. M. Murphy, personal communication, 1994). The impact of this choice was tested numerically by rerunning the $\tau = 0.2$ and $\tau = 1$ experiments for $Q_{abs}(IR)/Q_{ext}(Vis) = 0.4$ and $Q_{abs}(IR)/Q_{ext}(Vis) = 1$. In both cases, contrary to the $Q_{abs}(IR)/Q_{ext}(Vis) = 0.2$ case, the surface temperature is globally warmer in the $\tau = 1$ experiment, the enhancement of the greenhouse effect being larger than the diminution of the amount of solar energy reaching the surface. Note also that for increasing optical depths, the total condensation on the forming cap increases for $Q_{abs}(IR)/Q_{ext}(Vis) = 0.2$, is almost unmodified for $Q_{abs}(IR)/Q_{ext}(Vis) = 0.4$, and decreases for $Q_{abs}(IR)/Q_{ext}(Vis) = 1$, which provides an additional explanation for the difference between the present results and that published by *Pollack et al.* [1990].

The simulation with time-varying dust opacity was also rerun for $Q_{abs}(IR)/Q_{ext}(Vis) = 0.4$, which did not produce any significant improvement in terms of comparison with Viking seasonal pressure variations (experiment VAR2 in Table 3).

7. Best Fit Simulations

Method

The method we propose in order to fit Viking pressure data is based on the decomposition of the local surface pressure presented above: for Viking 1, for instance,

$$p_{VL1} = \alpha_{VL1} \times p_{atm} = \alpha_{VL1} \times (p_{tot} - p_N - p_S) \quad (9)$$

(in that section, we always refer to the eight-harmonic fit instead of the pressure variations themselves). Hopefully, the time evolution of α_{VL1}, which cannot be deduced from observation, is much less sensitive to the model parameters than $\alpha_{VL2/1}$. For all the low-resolution simulations with $\tau = 0.2$, this factor does not vary by more than 3%. Even the experiments with varying dust opacities are within this range, the effect of dust opacity on the value of α_{VL1} being maximum near northern summer solstice (Figure 25) when the atmosphere is clearest. Finally, for our best fit simulation, α_{VL1} is just taken from the simulation used as a basis for the best fit procedure.

We then take advantage of the high sensitivity of the atmospheric pressure to the ice albedo A and emissivity ϵ to fit the Viking 1 pressure variations by allowing, for the two caps, independent values of both parameters, (A_N, ϵ_N) and (A_S, ϵ_S) for the northern and southern cap, respectively. We also allow variations of the total amount (ice plus gas) of carbon dioxide p_{tot}. Assuming that the CO_2 trapped in one particular cap is to a first order independent of the total CO_2 amount p_{tot} and of the ice properties of the other cap, the mean surface pressure p_{atm} can be written as

$$p_{atm} = p_{tot} - p_N(A_N, \epsilon_N) - p_S(A_S, \epsilon_S) \quad (10)$$

The change δp_{atm} of the mean atmospheric pressure, resulting from small changes of these five parameters, can be written formally as

$$\delta p_{atm} = \delta p_{tot} - \delta A_N \frac{\partial p_N}{\partial A_N} - \delta \epsilon_N \frac{\partial p_N}{\partial \epsilon_N} - \delta A_S \frac{\partial p_S}{\partial A_S} - \delta \epsilon_S \frac{\partial p_S}{\partial \epsilon_S}. \quad (11)$$

The sensitivity functions, $\partial p_N/\partial A_N$, $\partial p_N/\partial \epsilon_N$, $\partial p_S/\partial A_S$, and $\partial p_S/\partial \epsilon_S$, computed from the results of the sensitivity experiments performed with $A = 0.4$–0.6 and $\epsilon = 0.6$–0.8 are shown in Figure 30. The functions themselves (thin curves) show rapid oscillations. This may be partly explained by the fact that the ice cover is not fractional: either a mesh is completely icy, or it is bare. If, due to a change in the ice parameters, the icing of a mesh occurs later or sooner, it makes a discontinuous change in the sensitivity. We retained smoothed functions (thick curves) for the best fit procedure.

The differences between the response to emissivity and albedo changes mentioned previously appears very clearly in Figure 30: at the beginning of the cap formation, an increase of the ice emissivity increases the mass of the cap about three times more than an equivalent increase of the ice albedo, whereas albedo and emissivity have an equivalent effect in the late recession period. This is especially important for our present purpose since, by acting independently on the four ice parameters, we act on functions which are strongly uncorrelated, with four maxima rather regularly distributed within a year.

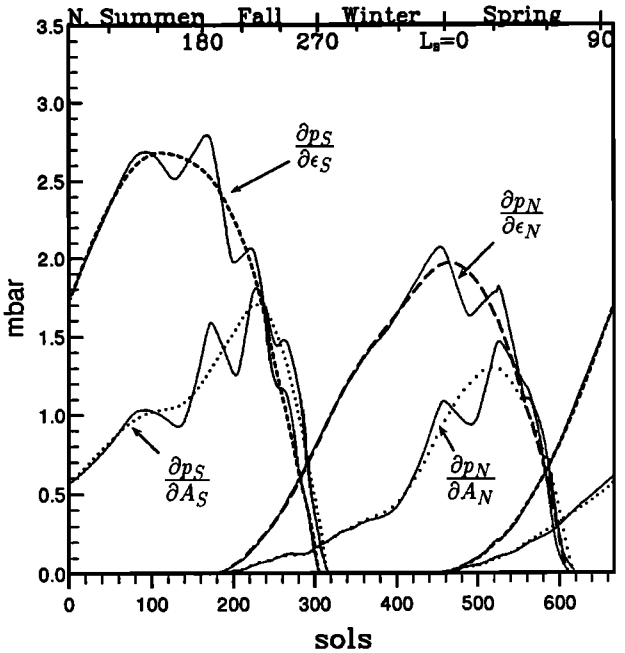

Figure 30. Sensitivity of the equivalent pressure of a given polar cap to a change of its albedo or emissivity, computed using the results of the sensitivity experiments presented previously. For instance, $\partial p_S/\partial A_S$ is computed as $[p_S(A_S = 0.6) - p_S(A_S = 0.4)]/0.2$. The thin lines correspond to the direct computation, and the thick (dotted or dashed) curves correspond to the smoothed functions used for the best fit procedure.

Finally, the best fit values of the parameters can be obtained by minimizing the following cost function measuring the difference between the simulated and observed pressures:

$$J(p_{\rm tot}, A_N, \epsilon_N, A_S, \epsilon_S) = \sum_{\rm sol=1}^{668} \left\{ p_{\rm VL1} - \alpha_{\rm VL1} \left(p_{\rm tot} - p_N - p_S - \delta A_N \frac{\partial p_N}{\partial A_N} - \delta \epsilon_N \frac{\partial p_N}{\partial \epsilon_N} - \delta A_S \frac{\partial p_S}{\partial A_S} - \delta \epsilon_S \frac{\partial p_S}{\partial \epsilon_S} \right) \right\}^2 \quad (12)$$

(where the sum is done with one value per day on one Martian year). The cost function J can be easily minimized by cancellation of its derivative which is equivalent to inverting a five-equation linear system. However, such a direct minimization produces extreme values of the emissivity and albedo. In fact, good fits could also be obtained by imposing one of the ice parameters. We thus introduce a supplementary constraint: we look for the fit which requires the minimum artificial asymmetry between the two hemispheres by adding to the cost function J a second term

$$\xi \left[(A_S - A_N)^2 + (\epsilon_S - \epsilon_N)^2 \right] \quad (13)$$

accounting for hemispheric asymmetries, where ξ represents the relative importance given to this asymmetry with respect to the departure from Viking 1 data (in fact, ξ has been normalized in order to have a transition region around $\xi = 1$). For very high values of ξ, we obtain the best fit with the same ice properties for both caps. For $\xi = 0$, we obtain the best unconstrained fit.

Once we have obtained, for a given value of ξ, a set of best fit parameters $p_{\rm tot}$, A_N, ϵ_N, A_S and ϵ_S, it is possible to compute a synthetic pressure curve at Viking 1 as

$$p = \alpha_{\rm VL1} \left(p_{\rm tot} - p_N - p_S - \delta A_N \frac{\partial p_N}{\partial A_N} - \delta \epsilon_N \frac{\partial p_N}{\partial \epsilon_N} - \delta A_S \frac{\partial p_S}{\partial A_S} - \delta \epsilon_S \frac{\partial p_S}{\partial \epsilon_S} \right) \quad (14)$$

Best Fit Results

We first present results of the best fit procedure applied to the control simulation. Figure 31 shows, for values of ξ varying from 10^{-3} to 10^4, the values of the best fit albedos and emissivities as well as the mean quadratic error between the synthetic and observed Viking 1 pressure. For $\xi < 1$, the best fit values are very different for the two caps, especially for albedo with $A_S = 0.3$ and $A_N = 0.65$. On the contrary, for large ξ, we find values of the ice parameters rather close the control values, with $\epsilon_S = \epsilon_N = 0.64$ and $A_S = A_N = 0.5$. Figure 32 shows the synthetic pressure at Viking 1 as obtained for $\xi = 0$, $\xi = 23$, and $\xi = 10^6$. Of course, the best agreement with Viking data (thin solid curve) is obtained for $\xi = 0$, but the agreement is still satisfactory for $\xi = 23$. The corresponding values of the ice parameters are given in Table 4. The difference $A_N - A_S$ is twice smaller for $\xi = 23$ than for $\xi = 0$. As expected also, it is mainly the first harmonic of the seasonal cycle which is sensitive to the value of ξ.

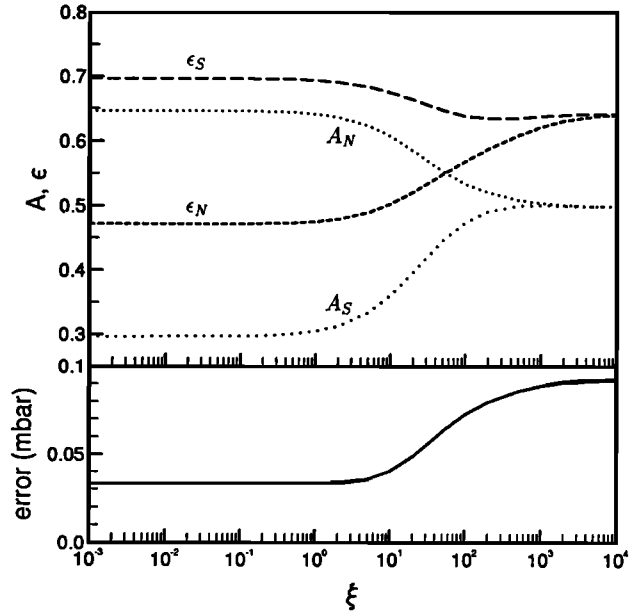

Figure 31. Best fit values of the ice albedo and emissivity computed for various values of the constraint coefficient ξ and the corresponding mean quadratic difference between the synthetic and observed Viking 1 pressure.

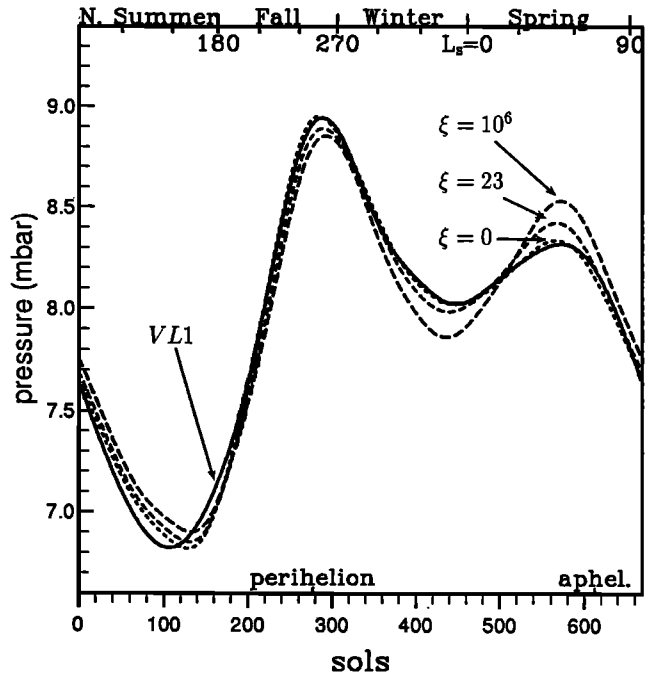

Figure 32. Three synthetic best fits for three different values of the constraint parameter ξ (10^6, 23, and 0). The pressure at Viking 1 is also shown (solid curve). All the curves correspond to eight-harmonic fits.

Table 4. Best Fit Parameters for $\xi = 0$, $\xi = 23$ and $\xi = 10^6$, and Mean Quadratic Error Based on the Low-Resolution Control Simulation

ξ	p_{tot}	A_N	ϵ_N	A_S	ϵ_S	Error, mbar
0	6.58	0.64	0.47	0.40	0.70	0.033
23	6.60	0.58	0.53	0.41	0.66	0.051
10^6	6.67	0.50	0.64	0.50	0.64	0.094

The best fit procedure was validated, a posteriori, by performing a new simulation analogous to the control simulation except that the ice parameters and total atmospheric mass were changed to the best fit values of the $\xi = 23$ case. The mean quadratic difference between the synthetic (deduced from the best fit algorithm) and simulated seasonal pressure evolutions is 0.035 mbar, which is surprisingly good in view of the simplicity of the best fit procedure.

The same approach was applied to the high-resolution simulation. Since the annual mass cycle is very close in the control and high-resolution simulations, we used the sensitivity functions computed from the low-resolution experiments. After some tests, we chose the $\xi = 10$ case ($p_{tot} = 6.152$ mbar, $A_N = 0.57$, $\epsilon_N = 0.53$, $A_S = 0.41$, and $\epsilon_S = 0.62$), which gives a mean quadratic error of 0.042 mbar, to perform a new high resolution simulation. The simulated pressure at Viking sites are presented in Figure 33.

Note that when we do not allow differences between the northern and southern ice properties, the best fit algorithm gives a mean quadratic error of 0.064 mbar only (much lower than for the low resolution) for $p_{tot} = 6.537$ mbar, $A = 0.51$, and $\epsilon = 0.58$.

The best fit procedure was also applied for other dust scenarios, some of which (like the $\tau = 1$ experiment) were closer to the Viking observations in terms of the two first harmonics of the seasonal cycle than for the control experiment. But at the same time, with more aerosols, the atmospheric mass budget is less sensitive to albedo or emissivity changes. As a consequence, all the best fits with high or time-varying dust opacities led to more extreme values of the ice emissivity and albedo.

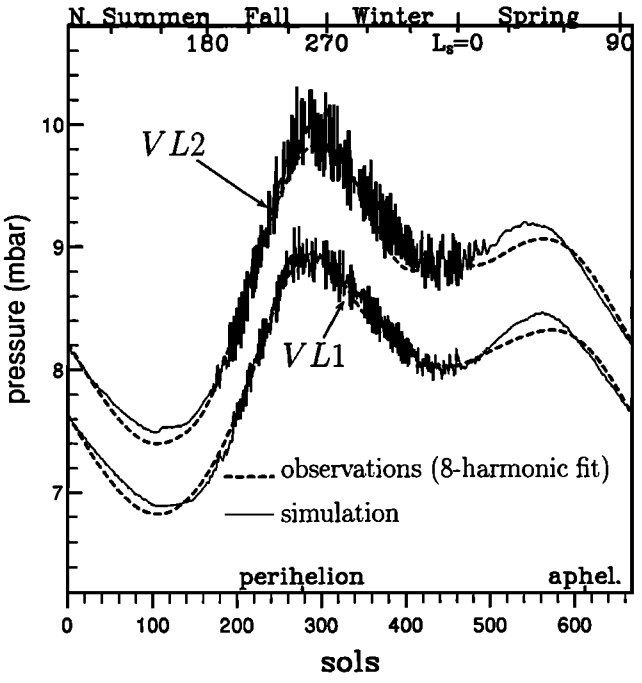

Figure 33. High-resolution best fit simulation ($p_{tot} = 6.152$ mbar, $A_N = 0.57$, $\epsilon_N = 0.53$, $A_S = 0.41$, and $\epsilon_S = 0.62$) of the pressure at the Viking sites and the observations smoothed by retaining the eight first harmonics of the seasonal cycle.

8. Concluding Remarks

Best Fit Parameters and Polar Processes

We have derived an algorithm which provides best fits to the Viking pressure seasonal cycle by varying independently the ice albedos and emissivities of the two polar caps. Thanks to the automatic procedure we use, we obtain values of the mean quadratic difference with Viking observations $\sigma \sim 0.04$–0.05 mbar when north-south asymmetries are allowed and $\sigma \sim 0.1$ mbar when identical values are imposed for the two caps. For comparison, the best fit published by *Pollack et al.* [1993] corresponds to $\sigma \sim 0.13$.

As *Wood and Paige* [1992] and *Pollack et al.* [1993] results, our study confirms the necessity for low values of the polar cap emissivity (of the order of 0.7). It also suggests the necessity for an asymmetry between the southern and the northern polar caps with a lower emissivity and larger albedo in the north. Note that, except for the $\tau = 1$ simulation, our best fit values of the cap albedo lie within the range of observations [see *Pollack et al.*, 1993, Table 4].

As already discussed, for instance, by *Pollack et al.* [1993], the necessity for low emissivity can be interpreted either in terms of real CO_2 ice properties or in terms of physical processes not accounted for in the model. Those low emissivity values are, at first approximation, compatible with the low values of the thermal emission recorded by the IRTM instrument aboard Viking orbiter, which have been recently analyzed extensively by F. Forget et al. (Low brightness temperatures of Martian Polar caps: CO_2 clouds or low emissivity?, manuscript in preparation, 1995).

If not due to a real low emissivity of the icy surface, this low thermal emission could be due for instance to opaque CO_2 clouds colder than the surface [*Pollack et al.*, 1990, 1993]. An alternative or additional explanation could arise from our rather poor knowledge of the polar orography. In fact, on the ice caps, there is a direct link, through the Clausius-Clapeyron law (2) and hydrostatic balance, between surface temperature and altitude variations:

$$\delta z = -\frac{L}{g}\frac{dT}{T} \sim -1.6 \times 10^5 \frac{dT}{T}. \qquad (15)$$

An underestimation by 1.6 km of the elevation of the

surface orography would correspond to an overestimation of the surface temperature in the model by about 1.4 K (the cap temperature being of the order of 140 K), which should be compensated, in order to reproduce good global condensation rates, by a decrease of the surface emissivity by 4%.

Improvements in our understanding of the polar atmospheric energy and mass budget on the polar caps will probably require more sophisticated parametrizations of the surface properties and atmospheric condensation, including the representation of CO_2–ice clouds, a careful comparison of the numerical results with the observations of the thermal emission by the Viking IRTM instruments as well as a better knowledge of the actual orography in the polar regions.

Interannual Variability and Dust

One intriguing result concerning the seasonal pressure variations recorded by the Viking landers is the very weak interannual variability. In particular, the pressure cycle was not significantly affected by the two global dust storms of the first Viking year, the temporary increase of the surface presure at Viking 2 during the second dust storm being mainly due to modifications of the dynamical component [*Pollack et al.*, 1993; paper 1].

For a given set of model parameters, the simulated interannual variability of the seasonal mass cycle is also very weak (see Figure 5) and compatible with observations, but, on the other hand, this cycle depends strongly on the atmospheric dust content, in a complex manner involving modifications of the radiative budget and atmospheric dynamics.

The link with observation is premature at this stage and would require a more realistic representation of the temporal and spatial variations of the atmospheric dust content. This could be achieved either by introducing in the model a climatology of the atmospheric dust content or by modeling directly the atmospheric dust transport in the GCM. It must also be kept in mind that the uncertainties on the dust optical properties can strongly affect both the seasonal pressure cycle and its sensitivity to changes of the atmospheric dust content.

Dynamical Contribution

The decomposition of the surface pressure variations into various components, already proposed in paper 1, has proved to be a powerful diagnostic tool for GCM simulations. The surface pressure appears to be especially sensitive to modifications of the dynamical component arising from modifications of the mean zonal winds following changes of the atmospheric angular momentum budget. This dynamical component is particularly sensitive to surface roughness and atmospheric dust content. Note that landing probes at 30° and 60° latitude in each hemisphere (the latitudes which are the most affected by the dynamical component) plus one at the equator would probably be optimum to constrain the dynamical component and, in turn, some model parameters and the annual mass cycle.

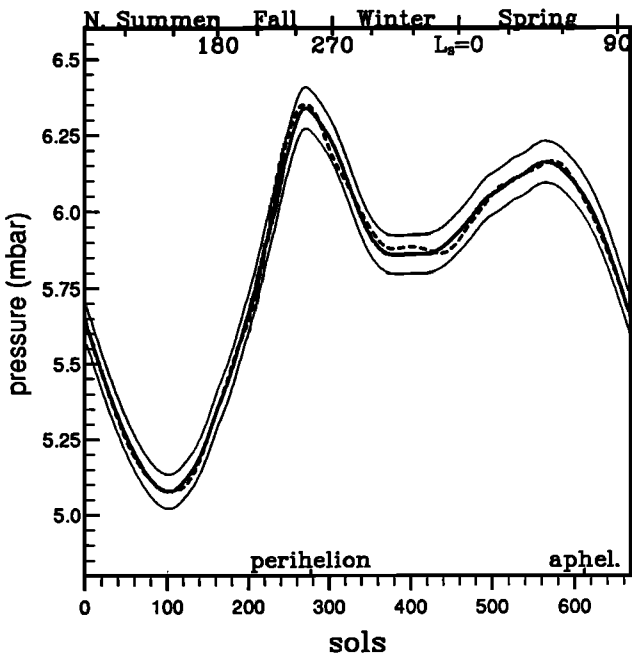

Figure 34. Planetary averaged surface pressure $p_{atm} = p_{VL1} \times \alpha_{VL1}$, where p_{VL1} is the eight-harmonic fit to the seasonal pressure variations observed by Viking 1 and α_{VL1} is taken from the high-resolution sensitivity experiment (dashed curve) and high-resolution best fit simulation (thick solid curve). The two thin solid curves have been computed by adding ±1.5% to the meteorological factor of the high-resolution best fit simulation.

One output of the present study is also the determination of the time evolution of the atmospheric mass from the Viking observations. Figure 34 shows the seasonal evolution of the planetary averaged surface pressure reconstructed from the Viking 1 pressure observations scaled by the meteorological factor α_{VL1} taken from the high-resolution sensitivity experiment (thick dashed curve) and best fit experiment (thick solid curve). The two thin curves, computed by adding ±1.5% to the meteorological factor of the best fit simulation, correspond to the maximum uncertainty estimated from the maximum variations of the meteorological factor in all the sensitivity experiments using a constant $\tau = 0.2$ or a time-varying dust optical depth.

Note also that the agreement of the simulated and observed relative pressure between the two Viking landers can be obtained only for a rather short range of values for the altitude difference between the two sites. The dashed curve in Figure 12 was computed assuming that Viking 2 was 980 m below Viking 1. A change by 50 m of this altitude difference would have shifted $\alpha_{VL2/1}$ by about 0.5%, resulting in a rather bad fit. This gives an estimation of the altitude difference: $\delta z = -980 \pm 50$ m.

Transient Eddies

The amplitude of the transient eddies in the clear-sky high-resolution simulation is in good agreement with Viking observations, except near northern winter sol-

stice, when it is strongly overestimated. The sensitivity experiments suggest that the increase of the dust optical depth during winter is responsible for the reduction of the transient activity in that season. In good agreement with Viking observations, this reduction is found to be stronger near northern winter solstice. Note also that the amplitude of the transient waves is much smaller in the southern hemisphere (not shown), as also found with the NASA/Ames GCM [*Barnes et al.*, 1993].

Implications for Spatial Exploration

We have mentioned above how GCM's can be used for the preparation of spacecraft missions, for instance, for the selection of landing sites which would lead to a better constraint of the atmospheric mass cycle and dynamical component.

It also appears clearly from the present study that one priority of the future Martian missions must be the determination of the Martian orography. An accurate knowledge of the orography is of prime importance both (1) for estimation of the energy budget over the caps, and (2) for fully efficient use of local pressure measurements, such as the Viking measurements.

This study underlines more generally the usefulness of using self-consistent models such as GCM's in conjunction with spacecraft observations. This approach could be made much more systematic by using the "data assimilation techniques" developed for the purpose of operational weather forecasting. For that goal, we are currently developing at LMD the adjoint of our Martian GCM, which we intend to use for four-dimensional variational assimilation [e.g., *Talagrand and Courtier*, 1987; *Thépaut and Courtier*, 1991] of the data of future Martian missions.

Acknowledgments. The computational means were provided by Institut du Développement et des Resources en Informatique Scientifique of Centre National de la Recherche Scientifique. The Viking pressure measurements were produced by *Tillman and Guest* [1987] and *Tillman* [1988] and provided to us by Steven Lee. They are available in digital form through the Planetary Data System. For information on ordering the data set(s) or related documentation, contact the PDS Planetary Atmospheres Discipline Node (303-492-5348; e-mail - Internet: lee@syrtis.colorado.edu, SPAN: ORION::LEE; Steven Lee, Laboratory for Atmospheric and Space Physics, University of Colorado, Boulder, CO 80309) or the PDS Central Node (818-306-6026; e-mail - SPAN: JPLPDS::PDS_OPERATOR; PDS Operator, Jet Propulsion Laboratory, MS 525-3610, 4800 Oak Grove Drive, Pasadena, CA 91109). We are also grateful to James Murphy and Robert Haberle for their useful comments on the first manuscript.

References

Barnes, J. R., Time spectral analysis of the midlatitude disturbances in the Martian atmosphere, *J. Atmos. Sci.*, *37*, 2002–2015, 1980.

Barnes, J. R., Midlatitude disturbances in the Martian atmosphere: A second Mars year, *J. Atmos. Sci.*, *38*(2), 225–234, 1981.

Barnes, J. R., J. B. Pollack, R. M. Haberle, R. W. Zurek, C. B. Leovy, H. Lee, and J. Schaeffer, Mars atmospheric dynamics as simulated by the NASA/Ames general circulation model, 2, Transient baroclinic eddies, *J. Geophys. Res.*, *98*(E2), 3125–3148, 1993.

Fouquart, Y., and B. Bonnel, Computations of solar heating of the Earth's atmosphere: A new parametrization, *Contrib. Atmos. Phys.*, *53*, 35–62, 1980.

Haberle, R. M., J. B. Pollack, J. R. Barnes, R. W. Zurek, C. B. Leovy, J. R. Murphy, H. Lee, and J. Schaeffer, Mars atmospheric dynamics as simulated by the NASA/Ames general circulation model, 1, The zonal-mean circulation, *J. Geophys. Res.*, *98*(E2), 3093–3124, 1993.

Hourdin, F., A new representation of the CO_2 15-μm band for a Martian general circulation model, *J. Geophys. Res.*, *97*(E11), 18,319–18,335, 1992.

Hourdin, F., P. Le Van, F. Forget, and O. Talagrand, Meteorological variability and the annual surface pressure cycle on Mars, *J. Atmos. Sci.*, *50*, 3625–3640, 1993.

James, P. B., H. H. Kieffer, and D. A. Paige, The seasonal cycle of carbon dioxide on Mars, in *Mars*, edited by H.H. Kieffer, B.M. Jakosky, C.W. Snyder and M.S. Matthews, pp. 934–968, University of Arizona Press, Tucson, 1992.

Keegan, K. D., J. E. Bachman, and D. A. Paige, Thermal and albedo mapping of the north polar region of Mars (abstract), *Lunar Planet Sci.*, *XXII*, 701–702, 1991.

Leovy, C., and Y. Mintz, Numerical simulation of the atmospheric circulation and climate of Mars, *J. Atmos. Sci.*, *26*, 1167–1190, 1969.

Louis, J.-F., A parametric model of vertical eddy fluxes in the atmosphere., *Boundary Layer Meteorol.*, *17*, 187–202, 1979.

Martin, T. Z., Thermal infrared opacity of the Mars atmosphere, *Icarus*, *66*, 2–21, 1986.

Martin, T. Z., and M. I. Richardson, New dust opacity mapping from Viking infrared thermal mapper data, *J. Geophys. Res.*, *98*(E6), 10,941–10,949, 1993.

Morcrette, J. J., L. Smith, and Y. Fouquart, Pressure and temperature dependence of the absorption in longwave radiation parametrizations, *Contrib. Atmos. Phys.*, *59*(4), 455–469, 1986.

Paige, D. A., and A. P. Ingersoll, Annual heat balance of Martian polar caps: Viking observations, *Science*, *228*, 1160–1168, 1985.

Paige, D. A., and K. D. Keegan, Thermal and albedo mapping of the south polar region of Mars (abstract), *Lunar Planet Sci.*, *XXII*, 1013–1014, 1991.

Paige, D. A., and S. E. Wood, Modeling the Martian seasonal CO_2 cycle, 2, Interannual variability, *Icarus*, *99*, 15–27, 1992.

Pollack, J. B., Properties and effects of Martian atmospheric dust, *Adv. Space. Res.*, *2*, 43–56, 1982.

Pollack, J. B., C. B. Leovy, P. W. Greiman, and Y. Mintz, A Martian general circulation model experiment with large topography, *J. Atmos. Sci.*, *38*, 3–29, 1981.

Pollack, J. B., R. M. Haberle, J. Schaeffer, and H. Lee, Simulations of the general circulation of the Martian atmosphere, 1, Polar processes, *J. Geophys. Res.*, *95*, 1447–1473, 1990.

Pollack, J. B., R. M. Haberle, J. R. Murphy, J. Shaeffer, and H. Lee, Simulation of the general circulation of the Martian atmosphere, 2, Seasonal pressure variations, *J. Geophys. Res.*, *98*(E2), 3149–3181, 1993.

Sadourny, R., and K. Laval, January and July performance of the LMD general circulation model, in *New Perspectives in Climate Modeling*, edited by A.Berger and C.Nicolis, pp. 173–197, Elsevier, Amsterdam, 1984.

Santee, M., and D. Crisp, Thermal structure and dust loading of the Martian atmosphere during late southern sum-

mer: Mariner 9 revisited, *J. Geophys. Res.*, *98*(E2), 3261–3279, 1993.

Sutton, J. L., C. B. Leovy, and J. E. Tillman, Diurnal variations of the Martian surface layer meteorological parameters during the first 45 sols at two Viking lander sites, *J. Atmos. Sci.*, *35*, 2346–2355, 1978.

Talagrand, O., and P. Courtier, Variational assimilation of meteorological observations with the adjoint vorticity equation, 1, Theory, *Q. J. R. Meteorol. Soc.*, *113*, 1331–1328, 1987.

Talagrand, O., F. Hourdin, and F. Forget, The LMD Martian general circulation model: Results about the annual pressure cycle, *Bull. Am. Astron. Soc.*, *23*, 1217, 1991.

Thépaut, J.-N., and P. Courtier, Four-dimensional variational data assimilation using the adjoint of a multilevel primitive-equation model, *Q. J. R. Meteorol. Soc.*, *117*, 1225–1254, 1991.

Tillman, J. E., Mars global atmospheric oscillations: Annually synchronized transient normal-mode oscillations and the triggering of global dust storms, *J. Geophys. Res.*, *93*(D8), 9433–9451, 1988.

Tillman, J. E., and W. Guest, Atmospheric pressure, point by point values: VL 1 sols 1-2245 and VL 2 sols 1-1050, technical report, National Space Science Data Center, Greenbelt, Md., 1987.

Tillman, J. E., N. C. Johnson, P. Guttorp, and D. B. Percival, The Martian annual atmospheric pressure cycle: Years without great dust storms, *J. Geophys. Res.*, *98*(E6), 10,963–10,971, 1993.

Wood, S. E., and D. A. Paige, Modeling the Martian seasonal CO_2 cycle: Fitting the Viking lander pressure curves, *Icarus*, *99*, 1–14, 1992.

F. Forget, F. Hourdin, and O. Talagrand, Laboratoire de Météorologie Dynamique du Centre National de la Recherche Scientifique, Ecole Normale Supérieure, 24 rue Lhomond, 75231 Paris cedex 05, France. (e-mail: hourdin@lmd.ens.fr, forget@lmd.ens.fr, talagran@lmd.ens.fr)

(Received March 14, 1994; revised October 21, 1994; accepted November 28, 1994.)